Associations Between Scattering Screens and Interstellar Medium Filaments

ASHLEY M. STOCK [ID][1, 2] AND MARTEN H. VAN KERKWIJK [ID][1]

[1]*David A. Dunlap Department of Astronomy & Astrophysics, University of Toronto, 50 Saint George St., Toronto, ON M5S 3H4, Canada*
[2]*Canadian Institute for Theoretical Astrophysics, University of Toronto, 60 Saint George Street, Toronto, ON M5S 3H8, Canada*

ABSTRACT

Pulsar scintillation can be used to measure small scale structure in the Galaxy, but little is known about the specific interstellar medium features that cause scintillation. We searched for interstellar medium counterparts to all scintillation screens for which absolute distances and scattering orientations have been measured – a sample of 12 pulsars and 22 screens. For one pulsar, PSR J0737-3039A, we re-analyze its scintillation screen and find evidence for a highly anisotropic screen. Among the screens, we found that eight are located inside of the Local Bubble, and a further six are less than 100 pc farther than its inner edge. Comparisons with tracers of ionized and magnetized media did not find any new associations. Instead, for seven of the pulsars analyzed, aligned H I filaments are seen for at least one of their screens, for a total of 12 out of 22 screens. This result seems unlikely to be due to chance: comparing with random trials, we estimate a likelihood of finding 12 or more screens with aligned emission by chance of only 0.004%. Estimating the significance of the amount of aligned emission (in standard deviations over the mean), the probability of finding as much observed aligned emission by chance is larger, at 1.7%, but still indicative of a real correlation. Since H I filaments are preferentially associated with cold neutral gas, and thus unlikely to cause scintillation, this may indicate both the filaments and the screens are aligned preferentially by the same mechanisms such as magnetic fields or shocks.

Keywords: Interstellar scintillation (855) — Pulsars (1306) — Interstellar medium (847)

1. INTRODUCTION

The interstellar medium (ISM) contains a rich assortment of structures such as clouds, filaments, shells, and bubbles. The structures' size distribution in the ISM has long been known to follow a power law, the "Big Power Law in the Sky". (e.g. Armstrong & Rickett 1981; Armstrong et al. 1995; Chepurnov & Lazarian 2010). At large scales, from 10^{16} to 10^{18} m, structures are observed directly, and the power law has been observed across multiple phases of the ISM, with the emission of cold, neutral hydrogen (e.g. Lazarian & Pogosyan 2000) as well as warm, ionized hydrogen (e.g. Chepurnov & Lazarian 2010). Below 10^{14} m the distributions are not observed directly, but rather inferred from the scattering of compact radio sources, such as pulsars and the cores of active galactic nuclei. From those indirect measure-

ments, the distribution has been suggested to extend all the way down to 10^6 m (Armstrong & Rickett 1981).

Compact radio sources are powerful probes of the ISM because they emit spatially coherent light. As the light propagates through the inhomogeneous ISM, it is scattered along many paths that interfere with each other, causing the intensity and phase of the light to vary with frequency and time as the source, observer, and scattering material move relative to each other. These variations, collectively known as scintillation, thus encode information about material along the line of sight to the source.

Scintillation is typically observed through the dynamic spectrum, which shows mean intensity as a function of frequency and time. Bright regions, called "scintles", have typical frequency widths of several kHz to MHz and durations on the order of minutes for pulsars and weeks for active galactic nuclei (AGN), when observed at GHz frequencies. The characteristic widths are quantified as the "decorrelation bandwidth" and "scintillation timescale", respectively (e.g., Cordes et al. 1985). Occasionally, "extreme scattering events" are seen (e.g.

Corresponding author: Ashley M. Stock

stock@astro.utoronto.ca

Fiedler et al. 1987), large changes in intensity that last much longer than the scintillation timescale and cover a much wider frequency range than the decorrelation bandwidth (indeed, they often are accompanied by changes in the scintillation timescale and decorrelation bandwidth).

Although scintillation gives information about the electron density and size distribution of the scattering medium, the nature of structures probed by scintillation remains poorly understood. Scintillation must occur in partially ionized gas, requiring electron densities likely higher than those in the molecular (too cold) and hot ionized (too tenuous) phases of the ISM, i.e., most likely in the warm neutral or warm ionized phases.

Clear parabolic structures in "secondary spectra", the power spectra of dynamic spectra, and, more directly, interferometric observations suggest the scattering is dominated by small numbers of localized, elongated structures (e.g., Rickett et al. 2009; Brisken et al. 2010). These structures are typically referred to as "screens", which may take the form of sheets or filaments. Sheet-like structures are particularly attractive, since if they are aligned nearly parallel to the line of sight, they appear filamentary and also solve the overpressure problem, i.e. that the scintillation and extreme scattering events require bending angles of order 10s of mas, which implies column density gradients of order $1000 \, \mathrm{cm}^{-2} \, \mathrm{cm}^{-1}$, and thus, for spherically symmetric structures, electron densities well higher than any expected in the ISM. In contrast, for a sheet sufficiently aligned with to the line of sight, typical ISM electron densities of $\sim 1 \, \mathrm{cm}^{-3}$ would suffice to cause the same bending angles (Pen & Levin 2014).

Under the assumption of thin, elongated screens, it is possible to model the distances, orientations of elongation, and velocities of screens. These properties can then be compared with properties of the ISM to potentially establish connections. Surveys of ISM tracers lack the resolution needed to observe directly structures on the scales that cause scintillation, but if the scattering screen is part of a larger scale structure, associations might still be found.

Early attempts to make associations used only sky positions and scattering strengths of the screens. For instance, extreme scattering events of quasars seem to be preferentially located near Galactic synchrotron filaments (loops) and near the edges of shell-like H I structures within those filaments (Fiedler et al. 1994). Scattering also appears enhanced for pulsars in the direction of Galactic Loop I, possibly due to interaction between Loop I and the Local Bubble (Bhat & Gupta 2002).

Using both sky positions and velocities of screens, Walker et al. (2017) found evidence that some screens were associated with hot stars. Specifically, they found that two variable sources, PKS 1322−110 and J1819+3845, had sight lines that passed within 2 pc of hot stars and for which the inferred velocities of the screens matched those of the stars. Walker et al. (2017) suggested that small, over-dense neutral clouds with tails ionized by hot stars might be responsible for the scintillation.

For a few pulsars, more direct associations between screens and specific ISM features have been made. The Crab pulsar, Vela pulsar, and PSR J0538+2817 are clearly scattered by their associated supernova remnants (Cordes et al. 2004; Sushch et al. 2011; Yao et al. 2021). One of the scattering screens towards PSR J1643−1224 is likely associated with an H II region, Sh 2−27 (Mall et al. 2022; Ding et al. 2023), while three of the scattering screens of PSR B1133+16 (McKee et al. 2022) and one of the scattering screens of B0656+14 (Yao et al. 2022) appear associated with the edge of the Local Bubble.

A previously unexplored avenue for understanding the physical nature of screens is their orientation. Measuring the orientation of screens generally requires interferometric techniques (e.g. Brisken et al. 2010), or observations over several months or years to fit for the annual and/or orbital variation in scattering properties (e.g. Rickett et al. 2014; Reardon et al. 2019; McKee et al. 2022). As a result, this has been done for very few pulsars so far. Yet, this measurement is needed to constrain the inclination of binary pulsars and could potentially be used to reduce errors in measurements of parallax by correcting for the positional shifts induced by the scattering.

In this paper, we use distances and orientations to investigate connections between scintillation screens and structures in the ISM, by correlating screen orientations with morphological features in tracers of different ISM environments. In Section 2, we outline the screens and ISM tracers used for comparison, and describe how we test for alignment. We discuss the screens for each pulsar in detail in Section 3, and consider the results from all screens in Section 4.

2. DATA AND ANALYSIS

2.1. *Scattering Screens*

We collected information on scattering screens from the literature, limiting ourselves to those with measurements of both distance and orientation of anisotropy. For all sources, we verified carefully how orientation is defined, and for PSR J0737−3039A we made new fits

to existing scintillation measurements (see Appendix for details). The results are summarized in Table 1. Further information can be found on-line in what we hope will become a live database[1], to which further screen distances and orientations will be added, such as those expected from the ongoing scintillation survey with with the Thousand Pulsar Array (Main et al. 2023).

2.1.1. Screen Orientations

The screen orientations in Table 1 are given East of North, and are measured along the long axis of the distribution of scattered images on the sky. This filament orientation equals that inferred from direct imaging and tracing annual arc curvature measurements; it corresponds to the direction of steepest change in density and phase. The orientation is perpendicular to what is inferred from scintillation timescales, which measure the direction associated with the longest scintillation timescale and thus that of least change in density and phase.

For an elongated set of scattering points, there is necessarily a 180° ambiguity in the orientation angle. We have chosen a convention in which the angle is between 0 and 180° so that the angle is towards the Eastern side of the long axis of the scattering points, adjusting the sign of the screen velocity appropriately if the original measurement from the literature followed a different convention (i.e., we ensured the screen velocity is positive if it has a positive component in right ascension).

2.1.2. Screen Kinematics

For most of the pulsars, information on the velocity of the screen is available. We only use the component of the velocity parallel to the structure's scattering points (see Table 1), since for elongated distributions of scattering points, there is little change in scintillation as one moves perpendicular to them, and hence any velocity in that direction is highly uncertain. Indeed, in some models for scintillation, such as those that require highly aligned sheets (Pen & Levin 2014), apparent variations perpendicular to the long axis of the scattering points are almost certainly due to different sheets at different distances.

For comparison with the measured velocities, we calculate the expected velocity for a structure following bulk Galactic rotation relative to the Local Standard of Rest, listing in Table 1 both the component parallel to the screen scattering points and the radial velocity – the latter for comparison with frequency-resolved ISM tracers. We calculate the expected value for the proper

motion and kinematic Local Standard of Rest velocity for a screen as:

$$v_\ell = d_s[B + A\cos(2\ell) - C\sin(2\ell)]\cos(b) \\ + U_0\sin(\ell) - V_0\cos(\ell), \tag{1}$$

$$v_b = -d_s[K + A\sin(2\ell) + C\cos(2\ell)]\sin(b)\cos(b) \\ + [U_0\cos(\ell) + V_0\sin(\ell)]\sin(b) - W_0\cos(b), \tag{2}$$

$$v_{\mathrm{LSRK}} = d_s[K + A\sin(2\ell) + C\cos(2\ell)]\cos(b), \tag{3}$$

where d_s is the distance to the screen from the Earth, and (ℓ, b) are its Galactic longitude and latitude. We used the Oort constants from Bovy (2017),

$$\begin{pmatrix} A \\ B \\ C \\ K \end{pmatrix} = \begin{pmatrix} 15.3 \pm 0.4 \\ -11.9 \pm 0.4 \\ -3.2 \pm 0.4 \\ -3.3 \pm 0.6 \end{pmatrix} \mathrm{km\,s^{-1}\,kpc^{-1}}, \tag{4}$$

and the velocity of the Sun relative to the Local Standard of Rest from Schönrich et al. (2010),

$$\begin{pmatrix} U_0 \\ V_0 \\ W_0 \end{pmatrix} = \begin{pmatrix} 11.1^{+0.69}_{-0.75} \\ 12.24^{+0.47}_{-0.47} \\ 7.25^{+0.37}_{-0.36} \end{pmatrix} \mathrm{km\,s^{-1}}. \tag{5}$$

2.2. ISM Tracers

Several ISM tracers were used to find structures with similar distance and/or orientation as the scattering screen.

Hα emission is a tracer of dense, warm ISM and H II regions, and might be expected to be correlated with higher electron densities. We used the composite all-sky map of Finkbeiner (2003) to identify structures. This map is composed of images from the Wisconsin Hα Mapper Sky Survey (WHAM-SS Haffner et al. 2003), the Virginia Tech Spectral-Line Survey (VTSS, Dennison et al. 1998), and the Southern H-alpha Sky Survey Atlas (SHASSA, Gaustad et al. 2001). Since many of our sources are at high Galactic latitudes, however, the Hα emission was often low or the surveys were incomplete. We found noticeable ISM structures only near PSR J0737−3039A and PSR J1643−1224.

Polarized emission can be used to trace ionized and magnetized ISM, which can emit polarized light or depolarize background polarized sources. We used the S-band Parkes All Sky Survey (S-PASS, Carretti et al. 2010) to search for ISM structures, but found that the features that could be seen were too diffuse or in regions of too low spatial resolution to provide meaningful comparisions with the screen orientations.

---

[1] https://github.com/scintillometry/screen-database

Table 1. Summary of associations between literature pulsar screens, Local Bubble, and H I filaments

Pulsar Name	Screen	Screen Orientation (°)	Screen Velocity (km/s)	Galactic Rotation (km/s)	Screen Distance (pc)	LB Distance (pc)	Predicted H I Radial Velocity (km/s)	Reference
J0337+1715	a	$66.1^{+3.7}_{-3.7}$	$4.25^{+0.44}_{-0.42}$	−10	$244^{+5.1}_{-3.1}$	139	−2.4	Gusinskaia et al. (in prep)
J0437−4715	a	134.6 ± 0.3	-31.9 ± 0.3	6.4	89.8 ± 0.4	287	0.5	Reardon et al. (2020)
	b	144 ± 6	-50 ± 6	−6.1	124 ± 3		0.7	
J0613−0200	2014+	16 ± 2	-1.2 ± 2.5	−5.9	300 ± 50	251	2.5	Main et al. (2020)
	2013	144 ± 9	-12.8 ± 2.8	3.3	330 ± 100		2.3	
J0636+5128	a	$96.98^{+3.16}_{-3.63}$	$-2.01^{+0.97}_{-1.15}$	−20.3	262^{+98}_{-38}	200	−3.5	Liu et al. (2023)
J0737−3039A	a	88.6 ± 4.3	-25.6 ± 1.5	3.3	260 ± 51	236	2.3	This Work
B0834+06	a	155 ± 1	-23 ± 1	−12.9	389 ± 5	265	3.9	Zhu et al. (2022)
	b	136 ± 1	-3.0 ± 3	−12.1	415 ± 11		4.2	
B1133+16	b	154^{+55}_{-37}	101^{+98}_{-169}	4.4	186^{+82}_{-87}	243	0.7	McKee et al. (2022)
	c	120^{+24}_{-23}	78^{+88}_{-47}	0.1	134^{+27}_{-31}		0.5	
	d	128^{+51}_{-39}	-399^{+230}_{-135}	8.4	197^{+67}_{-59}		0.8	
	e	135^{+50}_{-38}	-74^{+173}_{-142}	5.5	186^{+69}_{-73}		0.7	
	f	$11.3^{+2.4}_{-2.3}$	$-5.28^{+0.37}_{-0.42}$	−6.1	$5.47^{+0.54}_{-0.59}$		0.0	
J1141−6545	a	28.0 ± 0.4	$\cdots$	91.4	7200^{+300}_{-220}	159	−96.1	Reardon et al. (2019)
B1508+55[a]	a (weak)	39.8 ± 2.0	7.3 ± 1.4	3.9	127.1 ± 1.5	203	−0.1	Sprenger et al. (2022)
	a (strong)	52.4 ± 0.4						
	b	129.8 ± 2.0	2 ± 55	10.5	1940 ± 123		−1.0	
J1603−7202	a	140 ± 13	-5^{+15}_{-18}	−54.3	2500 ± 700	189	−44.9	Walker et al. (2022)
J1643−1224	a	150 ± 4	-10 ± 1	9.1	129 ± 15 [b]	91	−0.4	Mall et al. (2022)
	b	31 ± 9	-6 ± 3	−3.2	340 ± 9		−1.1	
J1909−3744	a	85 ± 6	14 ± 10	14.3	590 ± 50	195	−3.7	Askew et al. (2023)

NOTE—Screen Orientation gives the direction of the long axis of the distribution of scattering images, which equals the direction of greatest change in electron density of the scintillation screen (and thus perpendicular to possible associated extended physical structures); Screen Velocity is measured parallel to the direction of Screen Orientation unless otherwise indicated and is relative to the Solar System barycentre; Galactic Rotation is the expected transverse motion of gas relative to the Solar System barycentre in the direction of the Screen Velocity; LB Distance is distance from Earth to inner edge of Local Bubble wall from Pelgrims et al. (2020); Predicted H I Radial Velocity is the expected radial Local Standard of Rest velocity from Galactic rotation at the position of the screen. Screen distances are shown in blue if the screen is within the inner edge of the Local Bubble and red if outside of the inner edge of the Local Bubble by less than 100 pc.

[a] Screen a of this pulsar transitioned from weak to strong scattering which was modelled as a change in the screen orientation with other values fixed. Unlike other measurements, the screen velocity for screen a is given as the total magnitude of the screen transverse velocity rather than the projection of the velocity in the direction of the screen orientation. The direction of the screen velocity is $101 \pm 17°$ so the Galactic rotation is given as the projection along this direction. For full details see Sprenger et al. (2022).

[b] Associated with H II region, Sh 2-27, which is embedded in the shell of the Local Bubble

The cold and warm neutral medium are traced by H I and dust. Electron densities are (very) low, but correlation with scintillation screens might still occur if there are changes in electron density at boundaries with warmer, more highly ionized gas, or more generally if cold and warm gas are co-aligned, e.g., due to a magnetic field. For investigating H I emission, we used the Galactic All-Sky Survey (GASS, McClure-Griffiths et al. 2009; Kalberla et al. 2010; Kalberla & Haud 2015), Effelsberg-Bonn H I Survey (EBHIS, Winkel et al. 2016), and Galactic Arecibo L-Band Feed Array H I survey (GALFA-HI, Peek et al. 2011, 2018). In these surveys, sheet-like or filamentary structures are commonly seen, and we can compare these with screen orientations.

For dust emission, we used the 12, 25, and $60\,\mu$m IRIS all-sky maps (Miville-Deschênes & Lagache 2005). These maps showed similar morphology to the H I emission but are not resolved by velocity, so filaments appear more smoothed out. The similarity in morphology suggests that the filaments we observe in H I represent real density structures, as demonstrated by Clark et al.

(2019), rather than features of the turbulent velocity field, as suggested by, e.g., Lazarian & Yuen (2018).

Dust emission maps also include polarized intensity information, which correlates with the orientation of the Galactic magnetic field integrated along the line of sight. We explored this a little, but did not find any correlation. Similarly, we considered the Gaia-2MASS 3D dust maps (Lallement et al. 2019) as a way to compare with distances of screens, but our results were inconclusive. For completeness, we note that we also looked at CO maps (Dame et al. 2001), but found that those had too low a spatial resolution to identify filaments, and also covered only the Galactic plane and thus are available for only a few of our pulsars.

2.3. Filament Analysis

In our initial visual inspection, we noticed filamentary structure in H I that appeared aligned with the expected direction of lowest density gradient (i.e., perpendicular to the scattering point orientation) for PSR J0737−3039A, and hence our analysis focuses on H I filaments. However, we also looked for Hα filamentary structure for the two sources for which significant emission was seen, PSR J0737−3039A and PSR J1643−1224.

To identify filamentary structures and measure their orientation, we use the Rolling Hough Transform (RHT), developed by Clark et al. (2014). For each pixel in an image, the RHT counts the number of pixels within a window with diameter D_w that are correlated with each other along given orientations. The "RHT Spectrum" at that pixel position is then the fraction of correlated pixels along an orientation in the window, with only those over a threshold Z recorded. The threshold and window size, combined with the pixel scale Δx of a given survey, set a minimum filament size that can be identified, $ZD_w\Delta x$; we list relevant numbers for the different surveys in Table 2. For each of our pulsars, we look for filaments in the RHT spectrum at the sky position of the pulsar, and for the direction perpendicular to that of the scattering points.

In Figure 1, we show the H I emission data and associated RHT spectra for each pulsar. For each of the sources, we used the highest resolution H I survey available. For three sources (PSR J0337+1715, PSR B0834+06, and PSR B1133+16), data from both the GALFA-HI survey and EBHIS surveys were available. We found that the two surveys agreed on alignments for these, although the higher resolution made the GALFA-HI data superior, with more filaments identified and narrower ranges of orientation angle.

Table 2. Rolling Hough Transform Parameters and Survey Resolutions

	GASS	EBHIS	GALFA-HI
θ_{FWHM} (arcmin)	16	10	4
Δv_{LSRK} (km/s)	0.824	1.288	0.184^a
Δx (arcmin/pix)	5	3.26	1
RHT window D_w (pix)	45	45	60
Minimum filament size (deg)	1.87	1.22	0.54

Note—θ_{FWHM} is the angular and Δv_{LSRK} the spectral resolution of the survey. A Rolling Hough Transform threshold $Z = 0.5$ was used to calculate the minimum filament size.

[a]For the Rolling Hough Transform analysis, the data were rebinned to 1.288 km/s.

The H I data is resolved into velocity channels that give some information about the distance to the structures. The conversion between velocity and distance is complicated by the complex velocity structure of the gas, but still allows us to separate very distant emission from the mostly nearby structures that we are interested in. Hence, we include a velocity constraint in our requirements for alignment.

Note that because Galactic rotation does not change quickly with distance, each H I velocity channel includes information from several hundreds of parsecs of gas, potentially with overlapping filaments of differing orientations. In contrast, scintillation screens occur at specific locations along the line of sight, so these are unlikely to correlate well with averaged values of alignment (and indeed, we did not find evidence of correlation with orientation from dust polarization). This complicates the definition of alignment, especially for lines of sight with multiple screens.

2.4. Tests for Alignment

To determine where a screen is aligned with a filament, we need to define what constitutes being aligned, as well as to estimate how likely it is that the alignment is due to chance. We tried two methods, one where we set somewhat ad-hoc specific requirements, and another where we attempt to turn these constraints into a numerical score. For each method, we quantify the statistical significance by simulating 2,000 random screens for each real screen, with random orientation and positions randomly chosen in $5° \times 5°$ squares of the sky centred on the corresponding pulsar. A trial consists of one realization of a random screen for each real screen.

Note that the two methods effectively test different questions, viz., whether an aligned filament is present,
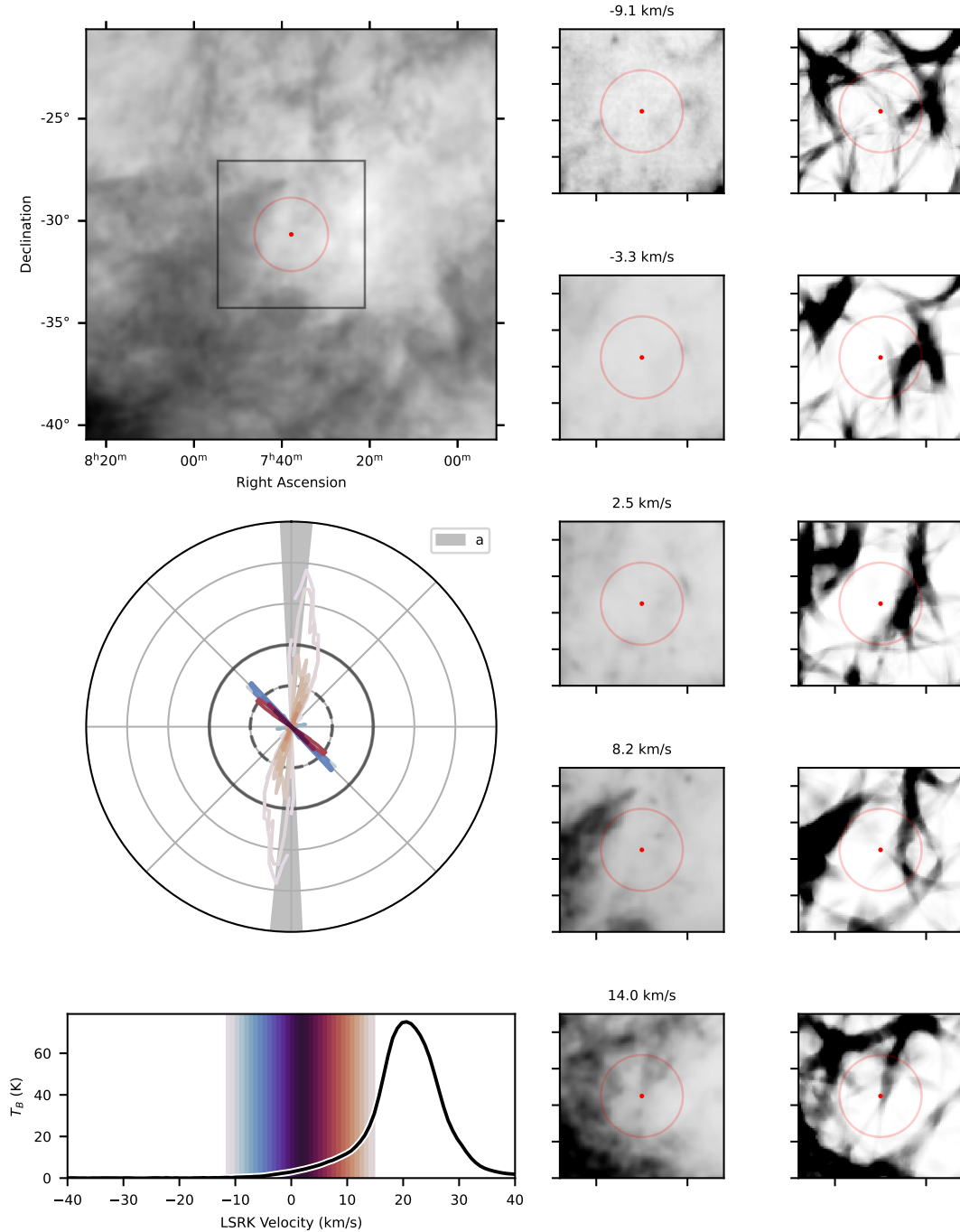
Figure 1. H I filaments near PSR J0737−3039A. The velocity channels around 14 km/s show a filament well aligned with the orientation of the pulsar's scattering screen. *Left column, top:* H I brightness temperature integrated over velocites between −11.5 and 14.8 km/s relative to the kinematic local standard of rest. The location of the pulsar is marked with a red dot, and the window for the Rolling Hough Transform analysis with a red open circle. *Left column, middle:* Rolling Hough Transform spectra at the position of the pulsar for a range of velocity channels, using colours from the panel below. The orientation of the pulsar's scattering screen is marked with a grey shaded region. *Left column, bottom:* H I line profile towards the pulsar, with a colour bar overlaid to show the velocity channels used above. *Middle column:* H I brightness temperature for different velocity channels (as labelled). The region covered is indicated by the inset box in the top left panel. *Right column:* Corresponding Rolling Hough Transform backprojections.

The complete figure set (10 images) is available in the online journal.

or whether the amount of aligned emission is significant. As we will see below, both methods suggest that the screens are likely associated with filaments, but the estimated probabilities of it being due by chance are quite different.

2.4.1. *Method 1: Specific Requirements for Alignment*

For our first method, we consider a filament aligned with a screen if:

1. Its velocity is within $\sim 13\,\mathrm{km/s}$ of that expected from Galactic rotation (19 velocity channels for EBHIS and GALFA-HI data, 33 velocity channels for GASS data), i.e., offset by no more than roughly the speed of sound (for all pulsars with multiple screens, this selects essentially the same velocity range for all screens);

2. The screen orientation is within $15°$ and the error in the screen orientation added in quadrature of a peak in the RHT spectrum (where $15°$ is a guess at the systematic uncertainties involved in estimating the filament orientation);

3. At least 70% of the pixels are aligned in one velocity channel; and

4. At least 60% of pixels are aligned in each of four contiguous channels.

Note that the last two conditions are similar to setting thresholds on the RHT, so this method is independent of choice of Z as long as $Z \leq 0.6$. The likelihood of a screen classification as aligned arising by chance was then determined from the fraction of random screens in a similar region of the sky that were classified as aligned. Similarly, the total likelihood of finding by chance as many screens aligned as observed, was determined from the number of trials where the number of aligned random screens were equal to or greater than the number of aligned real screens.

While this method is fairly straightforward, it is somewhat ad-hoc and sets hard cut-offs. Furthermore, it is biased towards finding alignment by comparison with only the closest peak in the RHT spectrum (though this should not affect probabilities, as the trials share this bias).

2.4.2. *Method 2: Using an Alignment Score*

To create a quantitative score for whether a screen is aligned, we use a procedure inspired by the above method: we convolve the RHT spectrum with a filter in both orientation and velocity, and look for peaks at the screen orientation angle. In orientation angle, to account for both the screen orientation measurement uncertainty $\delta\theta$ and our assumed systematic uncertainty of $15°$ in the orientation of the filament relative to that of a screen, we filter using a Gaussian with a width $\sigma = \sqrt{(15°)^2 + (\delta\theta)^2}$. For the velocity direction, to prioritize true filaments that extend over multiple velocity channels, we filter using a top hat with a width of four channels for the EBHIS and GALFA-HI data and six channels for the GASS data. For each real and random screen, we then find the maximum value of the filtered RHT spectrum at the observed screen orientation and calculate a score X of how many standard deviations above the mean of the filtered RHT spectrum the maximum is.

For each real screen, we estimate the probability $p_{\mathrm{scr},i}$ of its score arising by chance from the fraction of the random samples that has a higher value of X than the real screen. For all screens, we can then calculate a combined probability $p_{\mathrm{tot}} = \prod_i p_{\mathrm{scr},i}$ (i.e., the joint probability), and use fraction of the trials with higher p_{tot} as an estimate of the likelihood that screens and filaments seem aligned by chance.

To get a sense of the uncertainties in our estimates, we repeat the above procedure for two values of the threshold: our main choice, $Z = 0.6$, which aims to correspond to the threshold of method 1, and an extreme choice for comparison, $Z = 0$, i.e., simply counting the number of aligned pixels with positive flux.

3. RESULTS FOR INDIVIDUAL PULSARS

3.1. *PSR J0737-3039A*

This project began by investigating possible associations of structures in the interstellar medium with the scattering screen towards PSR J0737−3039A, a 23 ms pulsar in a binary with another, regular, 2.8 s pulsar, PSR J0737−3039B (Lyne et al. 2004). The ability to time both pulsars (until Pulsar B precessed out of sight in 2008), short orbital period of 2.4 hr, and eccentric orbit makes this system ideal for tests of general relativity. Accordingly, this system has been studied very well (e.g., Lyne et al. 2004; Kramer et al. 2006; Kramer et al. 2021a,b).

Several studies have also used the scintillation of PSR J0737−3039A to determine system and screen properties (Ransom et al. 2004; Stinebring et al. 2005; Rickett et al. 2014). An interesting surprise was that the secondary spectra of this pulsar seem to show only one arc, indicating a single dominant screen (Stinebring et al. 2005), even though the system is very close to the Galactic plane ($\ell = 245°, b = -4.5°$), and the line

of sight thus traverses gas with relatively large column densities and more complicated kinematics.

Rickett et al. (2014, R14 hereafter) used orbital and annual variations in the scintillation timescale to determine the screen distance and orientation, but found two different solutions, one more and one less asisotropic. To elucidate which one was better, we re-fit the scintillation timescales, choosing fit parameters somewhat better suited for constraining screen properties and using the updated pulsar timing ephemeris from Kramer et al. (2021b). Details of our fits are given in the Appendix, but here we simply note that the results are largely consistent with those of R14, with the biggest difference being the adopted pulsar distance (d_p): R14 used $d_p = 1.5$ kpc, based on the parallax measurement of Deller et al. (2009), while we use $d_p = 0.735$ kpc, the weighted average of parallax and timing parallaxes given by Kramer et al. (2021b). Since we find the same fractional distance, $s = 1 - d_s/d_p = 0.7$ (with d_s the distance of the screen), our fit places the screen closer, at $d_s = 260 \pm 50$ pc compared to the 450 pc inferred by R14.

We also found clearer evidence that the scattering screen is highly anisotropic, with its line of images nearly aligned with right ascension, at $\sim 88°6$ East of North. We made fits for several possible values of the inclination but found that these had very little effect on the screen properties; in Table 1, we list the result for what formally is our best fit, with an inclination of $i = 89°35$.

Comparing the screen orientation with H I surveys, we find possible alignment with an H I filament that spans velocities in the range of 14 to 27 km/s; see Figure 1. The radial velocities of the possibly aligned filament somewhat exceed the expected radial velocity from Galactic rotation (2.28 km/s). We note, however, that the tangential velocity of the scattering screen is also in excess of what is expected from Galactic rotation by a similar amount, 14 km/s. Despite the rather complex web of filaments in this section of the sky, the range of orientations identified with RHT is quite small. Applying the RHT to the Hα data did not identify filaments in front of PSR J0737−3039A.

For this particular pulsar, the evidence for the presence of an aligned H I filament is suggestive but in itself inconclusive: Method 1 finds similarly aligned filaments for 31.8% of the random trials, while Method 2 shows that for only 1.2% of the trials there is aligned emission equally or more significant than that for the pulsar for a threshold of 0.6 or a more similar 44.3% for a threshold of 0.0. The large discrepancy is likely due to this pulsar being close to the Galactic plane: while the line of sight to PSR J0737-3039A has only two clear filaments, many

of the randomly chosen nearby lines of sight have multiple filament orientations. Hence, they relatively easily fulfill the requirements for Method 1, which just looks for an aligned structure, while for Method 2, which also looks at the strength of of the aligned filament relative to others, those multi-filament trials are less likely to give a significant signal (at least if a cut-off is imposed). As will become clear for the other pulsars, this large a discrepancy between the two methods is not common, but it nevertheless shows how strongly the significance of a result can depend on the choice of detection criteria. Overall, we find the association suggestive.

One of the most prominent ISM structures along the line of sight to PSR J0737−3039A is the Gum Nebula. The Gum Nebula is a large, irregular shell with a radius of $22.7° \pm 0°1$ centred at a distance of about 450 pc (Purcell et al. 2015). It likely is an H II region with the shell resulting from the winds of hot stars in its interior (Purcell et al. 2015). The nebula and shell would have large density variations and thus likely favorable conditions for forming structures that could cause scintillation.

The distance to the Gum Nebula is inconsistent with the screen distance assuming roughly spherical geometry, although the irregular shape of the nebula could mean that it extends closer. Indeed, Kramer et al. (2021b) argue that PSR J0737−3039A is likely behind the Gum nebula, and suggest an extension of it, seen in emission near the pulsar's position, could be the source of the scintillation screen. This might be the case if this extension is substantially closer to us than the rest of the nebula, or if the distance to the pulsar's screen is larger, as would be the case if the pulsar were at a distance more like that inferred from the VLBI parallax and thus further away than indicated by timing.

The Gum Nebula's shell's expansion has been found to be slow and non-uniform, but the back face is expanding at 8.5 km/s while the front face is expanding at 14 km/s (Woermann et al. 2001). This expansion would suggest a filamentary structure on the front face of the nebula would have a radial velocity of about −11 km/s (after accounting for the motion of the centre of the nebula relative to Galactic rotation of 3.6 km/s used in Woermann et al. (2001)), which is inconsistent with the 14 to 27 km/s radial velocity of the potentially aligned filament.

While an association with the Gum Nebula may be possible, the screen distance is perhaps more suggestive of an association with the Local Bubble wall. Radial velocities of stars near the surface of the Local Bubble are around 5 to 9 km/s in excess of the Local Standard of Rest, and idealized modelling of the expansion of the Local Bubble gives a current expansion rate of $6.7^{+0.5}_{-0.4}$

km/s (Zucker et al. 2022). This is somewhat smaller than the velocity of the filament but in the same direction.

In summary, we find a neutral hydrogen filament that is aligned with the screen. There might be an association of the screen with either the Local Bubble or the Gum Nebula. Both also have significant H I components, with the Local Bubble wall defined by an increase in neutral gas and dust, and the Gum Nebula being surrounded by an H I shell. The distance to the scintillation screen and the velocity of the potentially aligned H I filament favour the Local Bubble wall.

3.2. PSR J0337+1715

PSR J0337+1715 is a millisecond pulsar in a hierarchical triple system. The pulsar is in a 1.6 day orbit with a white dwarf within a 327 day orbit of another white dwarf. The orbital parameters of this system are well known from pulsar timing and the effects of three-body interactions (Voisin et al. 2020). The screen parameters for this system were fit from nine years of scintillation measurements by Gusinskaia et al. (in prep).

There is substantial H I emission along the line of sight, but the orientation of the screen is not consistent with any identified H I filament. Indeed, while an aligned filament was found only for 5.3% of our trials for nearby lines of sight, the maximum observed amount of aligned emission is less than the mean, and higher maxima are found for 96.9% of the trials in method 2 (with $Z = 0.6$).

3.3. PSR J0437-4715

PSR J0437−4715 is a millisecond pulsar in a 5.76-day binary with a white dwarf. It has a precisely measured distance that places it very near to us, at 156.79 ± 0.25 pc (Reardon et al. 2016). Using 16 years of archival data, Reardon et al. (2020) was able to make precise measurements of two screens from arc curvature variations, with a primary screen at 89.8 ± 0.4 pc and a fainter, secondary screen at 124 ± 3 pc. Two other arcs were identified in the data, implying this pulsar has at least four screens, but there was insufficient signal to measure the properties of these additional screens (Reardon et al. 2020).

Some filamentary structure is identified in front of this pulsar that appears to be aligned with both screens. H I emission in the direction of this pulsar is very weak (peaking at ~ 1 K in 1.288 km/s channels), which could influence the reliability of identifying filaments. However, the H I morphology does not appear to be dominated by noise.

From our trials, the probability of finding a chance association for a single screen was quite large, at 37.3%.

The likelihood that both screens would be aligned by chance was found to be 4.9%, which looks more significant, but depends in part on the two observed screens having very similar orientation, while in the trials the orientations are randomized. For the trials, we found that 7.6% had stronger aligned emission than the nearer, primary screen, and 11.0% of trials showed stronger aligned filaments than the farther, secondary screen.

3.4. PSR J0613-0200

PSR J0613−0200 is a millisecond pulsar in a relativistic binary with a white dwarf companion in the Galactic plane (Lorimer et al. 1995). From a seven year dataset, Main et al. (2020) fit for the orientation and distance to its screen using scintillation arcs, ignoring the contribution of orbital motion to the velocity of the system. Increased scattering was observed in 2013 that could indicate a different screen. The arc measurements in 2013 were not fit well either by a model that assumed a single screen for the full seven year dataset nor when fitted separately, resulting in the large error in the distance to this screen. The best fits for both screens are shown in Table 1.

For both screens, we find possible aligned H I filaments. In this region of sky the likelihood to find at least one screen aligned by chance is 23.9% and the likelihood of two screens being aligned by chance is 1.7%. The latter may exaggerate the case for aligned filaments, however, given that filaments are identified in front of this pulsar over a wide range of angles. Indeed, we found that 50.7% of trials showed more significant aligned flux than the 2013 screen and 22.5% of trials showed more alignment flux than the 2014 and onwards screen. Hence, the association, like for most screens taken on their own, is rather tentative.

3.5. PSR J0636+5128

PSR J0636+5128 is a millisecond pulsar in a binary with a period of 1.6 hours (Alam et al. 2021). The properties of the screen were determined by Liu et al. (2022, 2023) using the scintillation timescale and decorrelation bandwidth from 2.5 years of data and ignoring the effect of the orbital motion (which is small for this system, so did not significantly decrease the quality of the fit).

There is substantial H I emission along the line of sight, with a clear filament identified between 2 and 10 km/s (exceeding the predicted radial velocity from Galactic rotation by 5 to 13 km/s). This filament, however, is not aligned with the screen but instead nearly perpendicular. The likelihood of finding a chance alignment along this line of sight is 20.9%, and 65.3% of trials showed more aligned emission than this screen.

3.6. *PSR B0834+06*

Using very long baseline interferometry (VLBI), Brisken et al. (2010) mapped the positions of images on the sky for the screens of PSR B0834+06. They identified a roughly 40 mas line of images corresponding to the main arc of the secondary spectra, as well as cluster of images offset by about 10 mas from the pulsar position. The cluster of images was suggested to be due to multiple scatterings of the light by the two screens (Liu et al. 2016), with the second screen terminating so that the pulsar was not seen through it. This model, which was confirmed in detail by the phase retrieval analysis done by Zhu et al. (2022), gives very accurate orientations.

There is a clear filament centred around 100° that is inconsistent with either screen. In this region of the sky the likelihood of finding at least one aligned screen by chance is 11.0%. Despite the lack of a specific aligned filament, only in 9.8% of the trials there was more aligned emission than what is seen for the main screen, i.e., the fainter filament visible in the RHT at the corresponding position angle is not entirely insignificant. In contrast, 36.6% of the trials had more aligned emission than was observed for the second screen.

3.7. *PSR B1133+16*

PSR B1133+16 is relatively nearby, at 372 ± 2 pc (Deller et al. 2019) and has displayed up to six different scintillation arcs (McKee et al. 2022). By tracing how those arcs changed with time over a 30 year baseline, McKee et al. (2022) found screen parameters for five screens. There are large error bars in the fitted values as often not all arcs can be seen and it is difficult to identify which arc corresponds to which screen. Although the relative brightness of the arcs vary with time, the scattering regions remains statistically similar over 30 years, placing a lower limit on the transverse width of the scattering region of $\sim 4''$, corresponding to a size of ~ 0.0035 pc at a distance of 186 pc.

For the purpose of our statistical analysis, we consider screens c, d, and e as one screen, since their orientations and expected radial velocities overlap. These screens all show probable alignment with hydrogen filaments. A filament is also found within the uncertainties of the orientation of screen f. The weak H I emission along this line of sight means that velocity channels with velocities above 5 km/s are dominated by noise and give unreliable but low percent orientations, below the 60% threshold used to determine alignment. The likelihood of chance alignment of at least one of three screens in this region of the sky is 10.2%, and 0.12% for at least two screens. We found that 77.3% of trials had stronger aligned emission than screen b (which was not considered aligned), 66.6%

had more than screen c/d/e, and 56.8% had more than screen f. Given the large error bars on the orientations of the screens, it is unsurprising that their alignment is not very significant.

3.8. *PSR J1141-6545*

PSR J1141−6545 is a millisecond pulsar in a relativistic binary with a white dwarf companion. Most of the orbital parameters of this pulsar are measured to high precision from pulsar timing. The distance to the pulsar, however, is less well constrained, but Reardon et al. (2019) fit the distance to the pulsar as well as screen properties from the scintillation timescale. Their best fit for the distance to the pulsar was 10^{+4}_{-3} kpc with a screen at $7.20^{0.30}_{-0.22}$ kpc. The fitting did not assume a one-dimensional screen, instead the screen was fit as an ellipse (using a method similar to that of Rickett et al. 2014). The axial ratio of the ellipse was found to be 2.14 ± 0.11, so the screen may not be very filamentary or may need to be described by more than one linear screen.

No filaments were identified in front of this pulsar in the velocity range searched. This is not surprising since the filaments at this distance are likely to be unresolved and hence the H I emission is low. Consequently, we do not include this pulsar in our statistical analyses.

3.9. *PSR B1508+55*

The secondary spectra of PSR B1508+55 usually display a single arc with flat arclets, which was explained as a result of two-screen scattering by Sprenger et al. (2022). The screen creating the main arc is nearby, at a distance of 127.1 ± 1.5 pc and the second screen is located close to the pulsar, at a distance of 1940 ± 123 pc (Sprenger et al. 2022). The morphology of the secondary spectra of this pulsar also appears to change, from a fuzzy arc to a thin arc with clear inverted arclets. This change in morphology is modelled as being caused by a change from strong to weak scattering of the closer screen, accompanied by a change in orientation from $142.4 \pm 0.4°$ to $129.8 \pm 2.0°$ (Sprenger et al. 2022). Sprenger et al. (2022) noted that the closer screen is 1.37 pc from the line of sight of an A2 star at a distance of 120 ± 8 pc, but found no candidate associations for the further screen.

A screen with orientation $142.4 \pm 0.4°$ is consistent with being aligned with an H I filament. However, this filament's orientation of approximately 144° is less consistent with the orientation of $121°\!.8 \pm 2°\!.0$ of the weak-scattering screen. The probability of finding at least one screen is aligned by chance in this region of the sky is 27.5%. Both screens showed much stronger

aligned emission than random trials, with only 9.9% of trials having stronger aligned emission than the weak-scattering screen and 1.5% of trials have more than the strong-scattering screen.

We do not find an alignment H I filament for the distant screen, but this may be expected: it may be too far away to be resolved and thus too faint. We thus exclude the distant screen from our statistical analysis.

PSR B1508+55 is quite distant ($2.10^{+0.13}_{-0.14}$ kpc) but has a very large proper motion (implying a velocity of 936^{+61}_{-64} km/s, Chatterjee et al. 2009). Given that the scintillation properties of PSR B1508+55 have changed as it crosses different ISM environments (Sprenger et al. 2022), one might worry about a mismatch in time. The EBHIS data was collected between 2010 and 2011, and Sprenger et al. (2022) used data from 2020 to 2022. Between 2011 and 2021 the pulsar would have moved $-0.74''$ in RA and $-0.62''$ in declination, i.e., much less than the pixel size of the EBHIS data. We therefore do not expect to see changes in the H I emission structure that would explain the changes in scintillation properties.

3.10. *PSR J1603−7202*

Walker et al. (2022) fit scintillation arc measurements for PSR J1603−7202. During the 12 years covered, PSR J1603−7202 displayed a significant increase in dispersion measure accompanied by decreases in scintillation timescale and decorrelation bandwidth, which Walker et al. characterize as an extreme scattering event. The dispersion measure then plateaued before decreasing to pre-event levels. Motivated by these changes in the line of sight ISM environment during their data set, Walker et al. (2022) allow for fits to different screens in different epochs. If only one screen is considered, their best fit orientation is $140 \pm 13°$ from Galactic North, at a distance of 2.47 kpc. For three screens, all had orientations consistent with $120°$, but with distances between 2.52 kpc and 3.33 kpc.

In Table 1, we include only the single screen model. Filaments identified with RHT are not consistent with orientations of either $140°$ or $120°$. However, given the large distances to the screen(s) it is not obvious that filaments would be resolved, and hence we exclude this pulsar from our statistical analyses.

3.11. *PSR J1643−1224*

PSR J1643−1224 is a millisecond pulsar in a 147 day orbit with a white dwarf companion, at a distance of 760 ± 16 pc (Desvignes et al. 2016). Using five years of scintillation arc measurements, Mall et al. (2022) modelled the scintillation screen(s) of PSR J1643−1224. The

secondary spectra for this pulsar displayed a single arc that appears to alternate between a thin arc, indicative of anisotropic screen, and a more diffuse arc that could in principle be indicative of either an isotropic screen or of multiple anisotropic screens. But scatter broadening of the pulsar image favours the solution with two anisotropic screens (Ding et al. 2023).

For comparison with H I filaments, we use the fit for two anisotropic screens. The distances of the two screens were 129 ± 15 and 340 ± 9 pc. The distance to the closer screen is consistent with that of the H II region, Sh 2-27, centred at 112 ± 3 pc (Ocker et al. 2020) with a diameter of 34 pc (Harvey-Smith et al. 2011).

Both screens have probable alignment with an H I filament. We also compared the orientation of screens with Hα filaments and, although filamentary structure was identified in front of this pulsar, the filaments were not aligned with the screens. The alignment with H I and not Hα could suggest that the changes in electron density responsible for the nearer screen do not arise in the H II region itself, but rather at, e.g., the interface with neutral hydrogen surrounding it. The likelihood that at least one of the screens is aligned by chance is 72.8%, and that of both being aligned is 23.9%. We found that 15.0% of trials had stronger aligned emission than the closer screen, while 85.1% of trials had stronger aligned emission than the farther screen.

3.12. *PSR J1909−3744*

PSR J1909−3744 is a very precisely timed millisecond pulsar due to its narrow pulse width, which has enabled a precise distance measurement, of 1.152 ± 0.003 kpc (Reardon et al. 2021). The pulsar is in a binary with white dwarf companion. The scintillation screen of PSR J1909−3744 was modelled using 13 years of scintillation arc measurements by Askew et al. (2023). They searched for nearby Hα sources and hot stars but found no associations.

We identify prominent filaments in front of the pulsar with orientations around $150°$, inconsistent with the orientation inferred for the scintillation screen. The likelihood of chance alignment for this line of sight is 28.2% and 24.8% of trials showed stronger aligned emission than this screen.

4. AGGREGATE RESULTS

4.1. *Filament Alignment*

We found that for six of the eleven pulsars analyzed there were possibly aligned H I filaments for at least one of their screens, for a total of 12 of 22 screens with possible alignments (see the summary in Table 3). All of the possible aligned screens were within 600 pc from

Earth, and all but one within 340 pc. There is an observational bias towards measuring the scintillation of less scattered, brighter pulsars which are typically nearby and therefore have nearby screens. The H I filament analysis is also biased towards nearby filaments since, for a given physical size, nearby filaments have larger angular size and are thus more easily identified.

We evaluated the significance of the probable alignment of the full sample of pulsars using the methods outlined in Section 2.4. We ignored screens that are greater than 1 kpc away and counted screens c, d, and e of PSR B1133+16 as one screen since they share the same orientation within their errors. With these adjustments, we are left with 17 screens, for 10 of which we found an aligned filament. Comparing this with our random trials, we found that only in 0.004% of those 10 or more screens were classified as having aligned filaments; for the trials, the expected number of aligned screens was 3.02. For the second method, which is based on the significance of the aligned flux, the evidence is less strong, but still highly suggestive: only 1.70% of the random trials showed more significant aligned flux than the real data using a threshold $Z = 0.6$ for the RHT. If the threshold is ignored, and the full RHT spectrum with a threshold of $Z = 0$ is used, then only 0.90% of our trials had more aligned flux than the real data. We thus conclude that the alignment of scintillation screens with H I filaments seen for our sample is unlikely to be due entirely to chance.

4.2. Screen Velocities

We compared the measured screen velocities with the expected velocity from Galactic rotation at the position of the screen (both values are listed in Table 1). The majority of screens (14 of 22) have velocities within 20 km/s of the Galactic rotation. Since the sound speed of the ISM is roughly 10 km/s (Goldreich & Sridhar 1995), the differences are not inconsistent with what is expected from random motion and/or slowly expanding or contracting interstellar medium, especially taking into account that most of the sample of screens are at high Galactic latitudes ($> 20°$ out of the plane), where motions are less well explained with Galactic rotation models.

Some exceptions to the screen velocities being comparable to the Galactic rotation velocities are the screens of PSR J0437−4715 and PSR B1133+16. For PSR J0437−4715, both screens are approximately 40 km/s in excess of the Galactic rotation. Since both are located inside the Local Bubble, this may simply reflect that this is a hot bubble blown by multiple supernova remnants (see below), in which higher velocities are

perhaps expected. For B1133+16, some of the best-fit screen velocities are even larger, at more than 70 km/s, but they also have large error bars, of more than 50%. Indeed, while four of the five screens have best-fit screen velocities more than 20 km/s in excess of Galactic rotation, only two (screens c and d) have velocities inconsistent with Galactic rotation within the 1σ uncertainties. Hence, while this hints at more rapidly moving ISM, the large uncertainties hinder any strong conclusions. It would seem worth measuring those velocities more accurately, e.g., using a dedicated VLBI campaign rather than relying on annual variations in arc curvature.

4.3. Local Bubble

We examine connections between the distances to the scintillation screens and the Local Bubble. The Local Bubble is a low density, irregularly shaped cavity with radius of $\sim 100 - 300$ pc filled with hot ($\sim 10^6$ K), mostly ionized gas surrounded by a thick wall (~ 100 pc) of dense, neutral gas. The Local Bubble is thought to have formed from a series of supernova shocks 10 to 15 million years ago, with surviving stars now located in the Sco-Cen association (Maíz-Apellániz 2001). Observations of nearby ($\lesssim 200$ pc) molecular clouds indicate they all lie at the surface of the Local Bubble with filamentary or sheet-like structure elongated along the surface of the bubble (Zucker et al. 2022). The density contrast and sheet-like structures, combined with Earth's location within the cavity, would seem to make the surface of the Local Bubble a highly favourable environment for scintillation.

To estimate distances to the inner edge of the Local Bubble, we use the model of Pelgrims et al. (2020) with 10 harmonic modes. The resulting distances along the line-of-sight for each of our pulsars are listed in Table 1. Along some lines of sight, particularly at higher Galactic latitudes, this model may overestimate the distance to the wall due to the resolution of dust map used in modelling. It also does not account for regions where the Local Bubble does not have a wall, sometimes referred to as a Local Chimney (e.g. Welsh & Lallement 2012).

Taking the distances at face value, we find that 11 of the 22 screens are within 100 pc of the Local Bubble wall, with five beyond and six in front of the nominal distance. However, three of the latter are located well within the cavity of the Local Bubble, more than 100 pc from its inner edge.

A particularly interesting case is PSR J0437−4715 which, at a distance of 156.79 pc, is itself located inside the cavity of the Local Bubble (the inner edge is at ~ 240 pc). It is perhaps surprising that many of the screens are located within the low density Cavity, but

Table 3. Summary of statistics

Pulsar	Screen	.. Method 1 .. Aligned?	(%)	Method 2 (Z = 0.6) X	(%)	Method 2 (Z = 0.0) X	(%)
J0337+1715	a	N	5.3	−0.4	96.9	−0.2	99.9
J0437−4715	a	Y	20.8	4.8	7.6	2.5	5.9
	b	Y	21.4	4.7	11.0	2.5	5.6
J0613−0200	2014+	Y	12.8	2.7	22.5	2.0	15.8
	2013	Y	12.8	1.4	50.7	1.4	56.6
J0636+5128	a	N	20.9	−0.3	65.3	0.7	53.6
J0737−3039A	a	Y	31.8	5.5	1.2	1.6	44.3
B0834+06	a	N	5.4	4.0	9.8	3.2	0.6
	b	N	5.9	1.9	36.6	1.8	21.4
B1133+16	b	N	3.4	1.2	77.3	0.9	66.7
	c/d/e	Y	3.8	1.5	66.6	0.8	78.2
	f	Y	3.5	0.9	56.8	1.0	58.1
B1508+55	a (weak)	N	14.6	3.6	9.9	2.2	6.4
	a (strong)	Y	15.0	4.8	1.5	2.6	1.1
J1643−1224	a	Y	48.3	3.5	15.0	2.2	14.6
	b	N	48.4	0.6	85.1	0.6	93.7
J1909−3744	a	Y	28.2	2.9	24.8	1.9	30.6
Combined probability			0.004		1.70		0.90

measurements of stellar absorption indicate several discrete clouds, even within 15 pc of Earth, that can cause scintillation of AGNs (Redfield & Linsky 2008; Linsky et al. 2008).

The H II region thought to cause the scintillation of the main screen of PSR J1643−1224, Sh 2-27, is located just outside of the Local Bubble, within the Ophiucus star formation region, where star formation is thought to have been triggered by the collision of the expanding Local Bubble with the surrounding ISM (Zucker et al. 2022).

5. CONCLUSION

Our results showed correlations between the orientations of scintillation screens and hydrogen filaments that are unlikely to be due entirely to chance. Our estimates of the likelihood of alignment vary between different methods (0.004% and 1.7%), but are both suggestive of a real association. If the correlation in alignment between scintillation screens and hydrogen filaments is physical, it implies there is correlation between alignment of ISM structures across many orders of magnitude of spatial scale – from the milli-arcsecond scales of scintillation to the degree scales of H I emission. Where there were overlapping H I surveys of different scales, it appeared that filaments were aligned in both the lower and higher resolution maps. However, higher resolution maps gave narrower orientations and more filaments. Even at the smallest resolution of 4 arcmin, the filaments did not ap-

pear to be resolved. This could impact the conclusions of alignment if substructure within filaments is not aligned with larger scale structure.

Scintillation requires fairly large gradients, $\gtrsim 10\,\mathrm{cm}^{-2}/\mathrm{cm}$ (Pen & Levin 2014), in the column density of electrons, but this may not translate to large volumetric electron density variations. Electron density gradients could be expected on the surfaces of cold neutral filamentary structures if they are embedded in warmer ISM, such that there is a transition from cold neutral to warm ionized phases creating a partially ionized skin on the filament. We did not see a correlation with Hα emission that would trace the warm ionized medium but this is, at least partially, due to insufficient spectral and angular resolution of the Hα maps.

The correlations in orientation of scintillation screens and H I filaments do not necessarily indicate a physical connection; instead, H I filaments could be tracers of the conditions that create scintillation screens. For instance, H I filaments appear to trace large-scale magnetic field orientation (Clark et al. 2014), and it seems plausible that the same magnetic field has ionized media aligned with it that may cause the scintillation (see for example Gwinn 2019), or that the scintillation occurs in magnetic reconnection sheets (Pen & Levin 2014).

Independently, our results suggests it is worthwhile to try to measure more screen orientations, and in particular try to improve the precision, e.g., using VLBI

(as so far done only for PSR B0834+06 by Brisken et al. 2010). Furthermore, higher-resolution H I studies would show more clearly whether filaments are truly associated with the scintillation regions, or simply trace similarly oriented structures.

Deeper understanding of the ISM environments for scintillation will require connections with multiple ISM tracers, ideally with true distances. While distances to ISM structures are generally not known, 3D ISM tomography is rapidly advancing, particularly in dust, allowing for detailed distance measurements of, e.g., the Local Bubble, as well as of more isolated H I filaments using the correlations between dust and H I. Similarly, our understanding of the 3-dimensional structure of the Galactic magnetic field is rapidly improving, which may provide another indication of what causes the scintillating structures.

ACKNOWLEDGMENTS

REFERENCES

Alam, M. F., Arzoumanian, Z., Baker, P. T., et al. 2021, ApJS, 252, 4, doi: 10.3847/1538-4365/abc6a0

Armstrong, J. W., & Rickett, B. J. 1981, MNRAS, 194, 623, doi: 10.1093/mnras/194.3.623

Armstrong, J. W., Rickett, B. J., & Spangler, S. R. 1995, ApJ, 443, 209, doi: 10.1086/175515

Askew, J., Reardon, D. J., & Shannon, R. M. 2023, MNRAS, 519, 5086, doi: 10.1093/mnras/stac3095

Astropy Collaboration, Robitaille, T. P., Tollerud, E. J., et al. 2013, A&A, 558, A33, doi: 10.1051/0004-6361/201322068

Astropy Collaboration, Price-Whelan, A. M., Lim, P. L., et al. 2022, ApJ, 935, 167, doi: 10.3847/1538-4357/ac7c74

Bhat, N. D. R., & Gupta, Y. 2002, ApJ, 567, 342, doi: 10.1086/338488

Bovy, J. 2017, MNRAS, 468, L63, doi: 10.1093/mnrasl/slx027

Brisken, W. F., Macquart, J. P., Gao, J. J., et al. 2010, ApJ, 708, 232, doi: 10.1088/0004-637X/708/1/232

Carretti, E., Haverkorn, M., McConnell, D., et al. 2010, MNRAS, 405, 1670, doi: 10.1111/j.1365-2966.2010.16608.x

Chatterjee, S., Brisken, W. F., Vlemmings, W. H. T., et al. 2009, ApJ, 698, 250, doi: 10.1088/0004-637X/698/1/250

Chepurnov, A., & Lazarian, A. 2010, ApJ, 710, 853, doi: 10.1088/0004-637X/710/1/853

Clark, S. E., Peek, J. E. G., & Miville-Deschênes, M. A. 2019, ApJ, 874, 171, doi: 10.3847/1538-4357/ab0b3b

Clark, S. E., Peek, J. E. G., & Putman, M. E. 2014, ApJ, 789, 82, doi: 10.1088/0004-637X/789/1/82

Cordes, J. M., Bhat, N. D. R., Hankins, T. H., McLaughlin, M. A., & Kern, J. 2004, The Astrophysical Journal, 612, 375, doi: 10.1086/422495

Cordes, J. M., Weisberg, J. M., & Boriakoff, V. 1985, ApJ, 288, 221, doi: 10.1086/162784

Dame, T. M., Hartmann, D., & Thaddeus, P. 2001, ApJ, 547, 792, doi: 10.1086/318388

Deller, A. T., Tingay, S. J., Bailes, M., & Reynolds, J. E. 2009, The Astrophysical Journal, 701, 1243, doi: 10.1088/0004-637x/701/2/1243

Deller, A. T., Goss, W. M., Brisken, W. F., et al. 2019, ApJ, 875, 100, doi: 10.3847/1538-4357/ab11c7

Dennison, B., Simonetti, J. H., & Topasna, G. A. 1998, PASA, 15, 147, doi: 10.1071/AS98147

Desvignes, G., Caballero, R. N., Lentati, L., et al. 2016, MNRAS, 458, 3341, doi: 10.1093/mnras/stw483

Ding, H., Deller, A. T., Stappers, B. W., et al. 2023, MNRAS, 519, 4982, doi: 10.1093/mnras/stac3725

Fiedler, R., Pauls, T., Johnston, K. J., & Dennison, B. 1994, The Astrophysical Journal, 430, 595, doi: 10.1086/174433

Fiedler, R. L., Dennison, B., Johnston, K. J., & Hewish, A. 1987, Nature, 326, 675, doi: 10.1038/326675a0

Finkbeiner, D. P. 2003, ApJS, 146, 407, doi: 10.1086/374411

Gaustad, J. E., McCullough, P. R., Rosing, W., & Van Buren, D. 2001, PASP, 113, 1326, doi: 10.1086/323969

Goldreich, P., & Sridhar, S. 1995, ApJ, 438, 763, doi: 10.1086/175121

Gusinskaia, N., van Kerkwijk, M. H., & Pen, U.-L. in prep

Gwinn, C. R. 2019, MNRAS, 486, 2809, doi: 10.1093/mnras/stz894

Haffner, L. M., Reynolds, R. J., Tufte, S. L., et al. 2003, ApJS, 149, 405, doi: 10.1086/378850

Harris, C. R., Millman, K. J., van der Walt, S. J., et al. 2020, Nature, 585, 357, doi: 10.1038/s41586-020-2649-2

Harvey-Smith, L., Madsen, G. J., & Gaensler, B. M. 2011, ApJ, 736, 83, doi: 10.1088/0004-637X/736/2/83

Hunter, J. D. 2007, Computing in Science Engineering, 9, 90, doi: 10.1109/MCSE.2007.55

Kalberla, P. M. W., & Haud, U. 2015, A&A, 578, A78, doi: 10.1051/0004-6361/201525859

Kalberla, P. M. W., McClure-Griffiths, N. M., Pisano, D. J., et al. 2010, A&A, 521, A17, doi: 10.1051/0004-6361/200913979

Kramer, M., Stairs, I. H., Manchester, R. N., et al. 2006, Science, 314, 97, doi: 10.1126/science.1132305

Kramer, M., Stairs, I. H., Venkatraman Krishnan, V., et al. 2021a, MNRAS, 504, 2094, doi: 10.1093/mnras/stab375

Kramer, M., Stairs, I. H., Manchester, R. N., et al. 2021b, Physical Review X, 11, 041050, doi: 10.1103/PhysRevX.11.041050

Lallement, R., Babusiaux, C., Vergely, J. L., et al. 2019, A&A, 625, A135, doi: 10.1051/0004-6361/201834695

Lazarian, A., & Pogosyan, D. 2000, ApJ, 537, 720, doi: 10.1086/309040

Lazarian, A., & Yuen, K. H. 2018, ApJ, 865, 59, doi: 10.3847/1538-4357/aad3ca

Linsky, J. L., Rickett, B. J., & Redfield, S. 2008, ApJ, 675, 413, doi: 10.1086/526420

Liu, S., Pen, U.-L., Macquart, J. P., Brisken, W., & Deller, A. 2016, MNRAS, 458, 1289, doi: 10.1093/mnras/stw314

Liu, Y., Verbiest, J. P. W., Main, R. A., et al. 2022, A&A, 664, A116, doi: 10.1051/0004-6361/202142552

Liu, Y., Main, R. A., Verbiest, J. P. W., et al. 2023, Science China Physics, Mechanics, and Astronomy, 66, 119512, doi: 10.1007/s11433-023-2182-6

Lorimer, D. R., Nicastro, L., Lyne, A. G., et al. 1995, ApJ, 439, 933, doi: 10.1086/175230

Luo, J., Ransom, S., Demorest, P., et al. 2019, PINT: High-precision pulsar timing analysis package, Astrophysics Source Code Library, record ascl:1902.007. http://ascl.net/1902.007

—. 2021, ApJ, 911, 45, doi: 10.3847/1538-4357/abe62f

Lyne, A. G., Burgay, M., Kramer, M., et al. 2004, Science, 303, 1153, doi: 10.1126/science.1094645

Main, R. A., Sanidas, S. A., Antoniadis, J., et al. 2020, MNRAS, 499, 1468, doi: 10.1093/mnras/staa2955

Main, R. A., Parthasarathy, A., Johnston, S., et al. 2023, MNRAS, 518, 1086, doi: 10.1093/mnras/stac3149

Maíz-Apellániz, J. 2001, ApJL, 560, L83, doi: 10.1086/324016

Mall, G., Main, R. A., Antoniadis, J., et al. 2022, MNRAS, 511, 1104, doi: 10.1093/mnras/stac096

McClure-Griffiths, N. M., Pisano, D. J., Calabretta, M. R., et al. 2009, ApJS, 181, 398, doi: 10.1088/0067-0049/181/2/398

McKee, J. W., Zhu, H., Stinebring, D. R., & Cordes, J. M. 2022, ApJ, 927, 99, doi: 10.3847/1538-4357/ac460b

Miville-Deschênes, M.-A., & Lagache, G. 2005, ApJS, 157, 302, doi: 10.1086/427938

Ocker, S. K., Cordes, J. M., & Chatterjee, S. 2020, ApJ, 897, 124, doi: 10.3847/1538-4357/ab98f9

Park, R. S., Folkner, W. M., Williams, J. G., & Boggs, D. H. 2021, AJ, 161, 105, doi: 10.3847/1538-3881/abd414

Peek, J. E. G., Heiles, C., Douglas, K. A., et al. 2011, ApJS, 194, 20, doi: 10.1088/0067-0049/194/2/20

Peek, J. E. G., Babler, B. L., Zheng, Y., et al. 2018, ApJS, 234, 2, doi: 10.3847/1538-4365/aa91d3

Pelgrims, V., Ferrière, K., Boulanger, F., Lallement, R., & Montier, L. 2020, A&A, 636, A17, doi: 10.1051/0004-6361/201937157

Pen, U.-L., & Levin, Y. 2014, MNRAS, 442, 3338, doi: 10.1093/mnras/stu1020

Price-Whelan, A. M., Sipőcz, B. M., Günther, H. M., et al. 2018, AJ, 156, 123, doi: 10.3847/1538-3881/aabc4f

Purcell, C. R., Gaensler, B. M., Sun, X. H., et al. 2015, ApJ, 804, 22, doi: 10.1088/0004-637X/804/1/22

Ransom, S. M., Kaspi, V. M., Ramachandran, R., et al. 2004, ApJL, 609, L71, doi: 10.1086/422911

Reardon, D. J., Coles, W. A., Hobbs, G., et al. 2019, MNRAS, 485, 4389, doi: 10.1093/mnras/stz643

Reardon, D. J., Hobbs, G., Coles, W., et al. 2016, MNRAS, 455, 1751, doi: 10.1093/mnras/stv2395

Reardon, D. J., Coles, W. A., Bailes, M., et al. 2020, ApJ, 904, 104, doi: 10.3847/1538-4357/abbd40

Reardon, D. J., Shannon, R. M., Cameron, A. D., et al. 2021, MNRAS, 507, 2137, doi: 10.1093/mnras/stab1990

Redfield, S., & Linsky, J. L. 2008, ApJ, 673, 283, doi: 10.1086/524002

Rickett, B., Johnston, S., Tomlinson, T., & Reynolds, J. 2009, Monthly Notices of the Royal Astronomical Society, 395, 1391, doi: 10.1111/j.1365-2966.2009.14471.x

Rickett, B. J., Coles, W. A., Nava, C. F., et al. 2014, The Astrophysical Journal, 787, 161, doi: 10.1088/0004-637x/787/2/161

Schönrich, R., Binney, J., & Dehnen, W. 2010, MNRAS, 403, 1829, doi: 10.1111/j.1365-2966.2010.16253.x

Sprenger, T., Main, R., Wucknitz, O., Mall, G., & Wu, J. 2022, MNRAS, 515, 6198, doi: 10.1093/mnras/stac2160

Stinebring, D. R., Hill, A. S., & Ransom, S. M. 2005, in Astronomical Society of the Pacific Conference Series, Vol. 328, Binary Radio Pulsars, ed. F. A. Rasio & I. H. Stairs, 349

Sushch, I., Hnatyk, B., & Neronov, A. 2011, Astronomy and Astrophysics, 525, A154, doi: 10.1051/0004-6361/201015346

Virtanen, P., Gommers, R., Oliphant, T. E., et al. 2020, Nature Methods, 17, 261, doi: https://doi.org/10.1038/s41592-019-0686-2

Voisin, G., Cognard, I., Freire, P. C. C., et al. 2020, A&A, 638, A24, doi: 10.1051/0004-6361/202038104

Walker, K., Reardon, D. J., Thrane, E., & Smith, R. 2022, ApJ, 933, 16, doi: 10.3847/1538-4357/ac69c6

Walker, M. A., Tuntsov, A. V., Bignall, H., et al. 2017, The Astrophysical Journal, 843, 15, doi: 10.3847/1538-4357/aa705c

Welsh, B. Y., & Lallement, R. 2012, PASP, 124, 566, doi: 10.1086/666503

Winkel, B., Kerp, J., Flöer, L., et al. 2016, A&A, 585, A41, doi: 10.1051/0004-6361/201527007

Woermann, B., Gaylard, M. J., & Otrupcek, R. 2001, MNRAS, 325, 1213, doi: 10.1046/j.1365-8711.2001.04558.x

Yao, J., Zhu, W., Manchester, R. N., et al. 2021, Nature Astronomy, 5, 788, doi: 10.1038/s41550-021-01360-w

Yao, J., Coles, W. A., Manchester, R. N., et al. 2022, ApJ, 939, 75, doi: 10.3847/1538-4357/ac9667

Zhu, H., Baker, D., Pen, U.-L., Stinebring, D. R., & van Kerkwijk, M. H. 2022, arXiv e-prints, arXiv:2208.06884. https://arxiv.org/abs/2208.06884

Zucker, C., Goodman, A. A., Alves, J., et al. 2022, Nature, 601, 334, doi: 10.1038/s41586-021-04286-5

APPENDIX

A. PROPERTIES OF THE SCINTILLATION SCREEN OF PSR J0737−3039A

We make a new fit for the scintillation screen properties of PSR J0737−3039A based on the scintillation timescale data and analysis of Rickett et al. (2014), hereafter referred to as R14. This new fit was motivated by two factors: (1) the original work found a rather large scintillation screen velocity, especially for the most anisotropic case (> 100 km/s); and (2) the pulsar timing measurements of this pulsar were recently updated by Kramer et al. (2021b), including a significantly different distance to the pulsar. Below, we outline the details of the model we use, following the description and nomenclature of R14, and present the results of the fits.

A.1. *Scintillation Model*

The scintillation timescale, T_{ISS}, is the time it takes for the auto-correlation function of the source brightness to fall by a factor e. Hence, the scintillation timescale depends on the spatial scale of phase changes on the screen, known as the mean diffractive scale (s_0), as well as the relative velocities of the source, observer, and screen.

The velocity of the line of sight can be decomposed into the barycentric velocity of the pulsar binary, $\mathbf{V}_{\mathrm{C}}$ and the orbital velocity of the pulsar. The barycentric velocity is given by,

$$\mathbf{V}_{\mathrm{C}} = \mathbf{V}_{\mathrm{P}} + \mathbf{V}_{\mathrm{E}}s/(1-s) - \mathbf{V}_{\mathrm{IS}}/(1-s), \tag{A1}$$

where $\mathbf{V}_{\mathrm{P}}$ is the proper motion of the pulsar center of mass, $\mathbf{V}_{\mathrm{E}}$ is the velocity of Earth, $\mathbf{V}_{\mathrm{IS}}$ is the velocity of the screen and $s = 1 - (d_{\mathrm{screen}}/d_{\mathrm{psr}})$ is the fractional distance from the pulsar to the screen. This velocity is related to the commonly used "effective velocity" as $\mathbf{V}_{\mathrm{C}} + \mathbf{V}_{\mathrm{P,orbital}} = \mathbf{V}_{\mathrm{eff}}/(1-s)$.

The orbital motion is most easily calculated in the reference frame of the pulsar orbit, defined such that $\hat{z}$ points from the Sun to the barycentre of the orbit, $\hat{x}$ is aligned with the line of nodes of the pulsar orbit, and $\hat{y} = \hat{z} \times \hat{x}$. The transformation from equatorial coordinates to the pulsar orbital frame is done by rotating the velocities by the longitude of ascending node, Ω, which is a free parameter. The geometry of the model is shown in Figure 2. In x-y coordinates, the average orbital velocity is given as $(V_o e \sin \omega, V_o e \cos \omega \cos i)$, where ω is the argument of periastron. V_o is the average orbital speed, given as $V_o = 2\pi a/(P_{\mathrm{b}}\sqrt{1-e^2})$ where a is the semimajor axis of the orbit, P_b is the orbital period, and e is the eccentricity of the orbit.

To determine screen parameters from the orbital harmonic coefficients, a single, potentially anisotropic scattering screen is assumed. The anisotropy of the screen is described by its axial ratio, A_{R}, and the orientation of its major axis, ψ_{AR}. Since A_{R} is unbounded, R14 define a variable $R = (A_{\mathrm{R}}^2 - 1)/(A_{\mathrm{R}}^2 + 1)$ which ranges from 0 (isotropic) to 1 (linear). These parameters are contained within the following variables:

$$a = \left[1 - R\cos(2\psi_{\mathrm{AR}})\right]/\sqrt{1-R^2},$$
$$b = \left[1 + R\cos(2\psi_{\mathrm{AR}})\right]/\sqrt{1-R^2},$$
$$c = -2R\sin(2\psi_{\mathrm{AR}})/\sqrt{1-R^2}. \tag{A2}$$

The scintillation timescale will depend on the orbital angle ϕ (which, like R14, we define relative to the line of nodes, as $\phi = \theta + \omega$, with θ the true anomaly). This dependence can be fitted by five orbital harmonic coefficients $(K_0, K_S, K_C, K_{S2}, K_{C2})$ as

$$T_{\mathrm{ISS}}(\phi) = K_0 + K_S \sin(\phi) + K_C \cos(\phi) + K_{S2} \sin(2\phi) + K_{C2} \cos(2\phi). \tag{A3}$$

The orbital harmonic coefficients are defined in terms of the physical parameters as,

$$
\begin{aligned}
K_0 =& [0.5\, V_o^2(a + b\cos^2 i) + a(V_{\mathrm{C}_x} - V_o e \sin \omega)^2 + b(V_{\mathrm{C}_y} + V_o e \cos \omega \cos i)^2 \\
& + c(V_{\mathrm{C}_x} - V_o e \sin \omega)(V_{\mathrm{C}_y} + V_o e \cos \omega \cos i)]/s_{\mathrm{p}}^2 \\
K_{\mathrm{S}} =& - V_o[2a(V_{\mathrm{C}_x} - V_o e \sin \omega) + c(V_{\mathrm{C}_y} + V_o e \cos \omega \cos i)]/s_{\mathrm{p}}^2 \\
K_{\mathrm{C}} =& V_o \cos i[c(V_{\mathrm{C}_x} - V_o e \sin \omega) + 2b(V_{\mathrm{C}_y} + V_o e \cos \omega \cos i)]/s_{\mathrm{p}}^2 \\
K_{\mathrm{S2}} =& - 0.5cV_o^2 \cos i/s_p^2 \\
K_{\mathrm{C2}} =& 0.5V_o^2(-a + b\cos^2 i)/s_{\mathrm{p}}^2.
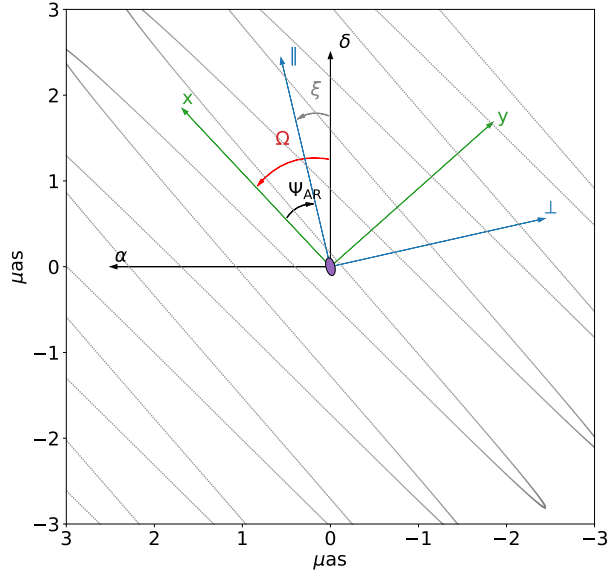\end{aligned}
\tag{A4}
$$

Figure 2. Schematic showing the coordinate systems used. The $x - y$ plane is oriented with x along the line of nodes of the orbit. It has its origin at the equatorial coordinates α, δ of the pulsar, but is rotated East of North (around equatorial coordinates) by the longitude of ascending node, Ω. The direction parallel to the semi-major axis of the screen resolution is rotated counterclockwise from the x axis by the angle, ψ_{AR}. The orientation of the screen as seen from Earth, ξ, is measured East of North, again defined as that of the long, "parallel" axis. The screen resolution element is shown in purple for an axial ratio of 2.06, corresponding to an anisotropy parameter of $R = 0.62$. It is to scale for an observation at 820 MHz and a distance of 262 pc (using the fractional distance to the screen of $s = 0.643$ and a pulsar distance of 735 pc). For comparison, the projected path of the pulsar over eight orbits is shown for $i = 89°.35$, using grey dots, each separated by ten seconds. Note that it is the parallel direction along which to expect any filamentary structure, but it is the perpendicular direction along which the scintillation timescale changes fastest, and for which the screen velocity can be best constrained.

Here, the size of the resolution element of the screen, s_p, is related to the mean diffractive scale, s_0 by $s_p = s_0/(1-s)$.

Since the mean diffractive scale is frequency dependent, scintillation timescales of data from observations in different frequency bands cannot be directly compared. In order to combine data, R14 used normalized orbital harmonic coefficients ($k_0 = K_0/K_{C2}$, $k_s = K_S/K_{C2}$, etc.), which are independent of the mean diffractive scale.

In our fits, we depart from the fitting method used in R14 in two ways, to minimize the effect of covariances on the properties of the screen. First, we fit directly for the angle ξ of the scintillation screen on the sky (measured East from North, and constrained to fall in the range 0 to 180°), making the orientation $\Omega = \xi + \psi_{AR}$ of the pulsar orbit a derived parameter (rather than vice versa). This is because orbital motion directly constrains relative orientations between the screen and the orbits: ψ_{AR} for the pulsar, and ξ for the Earth. Indeed, in the fits from R14, one sees that Ω and ψ_{AR} are strongly correlated, while their difference $\Omega - \psi_{AR} = \xi$ is well constrained.

Second, we represent the velocity of the screen in directions parallel and perpendicular to the screen's semi-major axis rather than along the orbital x and y coordinates as done in R14. This is because in the limit that $R \to 1$ (i.e. a one-dimensional screen) the scintillation timescale is completely independent of motion parallel to the screen orientation, and hence the velocity along this direction becomes indeterminate. By using velocity components in the screen coordinates, this uncertainty is directly captured by the fits, while in any other coordinate system, the velocities and uncertainties in both directions would be affected by it.

A.2. *Data and Fitting*

We fit for physical parameters of the pulsar and scattering screen using the normalized orbital harmonic coefficients presented in R14. These coefficients were measured from 17 observations taken between December 2003 and July 2005,

Table 4. Fitted Parameter, with 1σ credible intervals

Parameter	.... $\cos i > 0$		.... $\cos i < 0$		.... i free	
	$V_{\mathrm{IS},\parallel}$ free	$V_{\mathrm{IS},\parallel} = 0$	$V_{\mathrm{IS},\parallel}$ free	$V_{\mathrm{IS},\parallel} = 0$	$V_{\mathrm{IS},\parallel}$ free	$V_{\mathrm{IS},\parallel} = 0$
i (deg)	89.35	89.35	90.65	90.65	87.8 ± 1.2	88.85 ± 0.54
s	0.646 ± 0.040	0.665 ± 0.031	0.614 ± 0.047	0.613 ± 0.045	0.708 ± 0.013	0.695 ± 0.023
ξ (deg) [a]	178.6 ± 4.3	11.9 ± 4.7	174.2 ± 3.0	167.6 ± 3.9	176.3 ± 3.7	15.8 ± 5.0
R	0.87 ± 0.11	0.63 ± 0.14	0.969 ± 0.057	0.840 ± 0.083	0.76 ± 0.17	0.44 ± 0.19
ψ_{AR} (deg)	43 ± 10	34.9 ± 7.0	141.5 ± 8.9	148.7 ± 7.0	73 ± 13	43.6 ± 9.2
$V_{\mathrm{IS},\perp}$ (km/s)	-25.6 ± 1.5	23.7 ± 1.3	-23.6 ± 1.9	-21.9 ± 1.3	-25.3 ± 1.7	25.3 ± 1.4
$V_{\mathrm{IS},\parallel}$ (km/s)	-46 ± 36	0	100 ± 120	0	-47 ± 28	0
N_{dof}	58	59	58	59	57	58
χ^2_ν	1.88	1.85	2.15	2.30	1.81	1.95
d_s (pc) [b]	260 ± 51	246 ± 23	284 ± 55	284 ± 33	215 ± 18	224 ± 17
Ω (deg)	42 ± 11	47 ± 12	136 ± 12	136 ± 11	69 ± 10	59 ± 14

[a] Screen orientation measured east from declination axis

[b] Screen distance uses pulsar distance $d_p = 735 \pm 60$ pc

using the 100 m Robert C. Byrd Green Bank Telescope at either 1850 MHz with a bandwidth of 800 MHz or 820 MHz with a bandwidth of 50 MHz. For details about the observations and data reduction, see R14.

For the velocity of the Earth, $\mathbf{V}_{\mathrm{E}}$, we used the JPL DE401 ephemeris (Park et al. 2021). The Earth velocity was calculated only for the beginning of the observation since the change in Earth velocity during an observation is very small. The interstellar plasma velocity, $\mathbf{V}_{\mathrm{IS}}$, and the fractional distance to the screen, s, were assumed to be constant between all epochs. Orbital phases and scales for pulsar A were inferred using PINT (Luo et al. 2019, 2021), using the parameter file from Kramer et al. (2006) for comparison with R14, and that from Kramer et al. (2021b) for the results presented here. Measurements of Shapiro delay constrain the value of $\sin i$ but are degenerate with the sign of $\cos i$. Like R14, we fit the scintillation timescales with the inclination fixed for both signs of $\cos i$ as well as fitting i as a free parameter. The inclinations used were $i = 88.7°$ or $91.3°$ from Kramer et al. (2006), and $i = 89.35°$ or $90.65°$ from Kramer et al. (2021b).

A.3. *Results*

To test our fitting routine, we first used parameters like in R14. We found consistent results, except that our calculated reduced chi-squared values (χ^2_ν) differed somewhat, for reasons we do not quite understand but possibly simply related to having somewhat different codes and ephemerides. For all further fits, we used the updated pulsar timing values from Kramer et al. (2021b). These give very similar results, which is not unexpected, since for our purposes, all parameter changes except for the distance are relatively small.

One of the biggest changes in the new timing parameters for PSR J0737−3039A is the distance to the pulsar. In our fit setup, the only effect of changing the pulsar distance is that it changes the systemic velocity of the pulsar binary, $\mathbf{V}_{\mathrm{P}}$. R14 used $V_{\mathrm{P}\alpha} = -17.8$ km/s and $V_{\mathrm{P}\delta} = 11.6$ km/s based on the distance of $1.15^{+0.22}_{-0.16}$ kpc determined by Deller et al. (2009). More recent astrometry yields a distance of 770 ± 70 pc, while the parallax inferred from timing implies 465^{+134}_{-85} pc (Kramer et al. 2021b). As in Kramer et al. (2021b), we adopted a weighted mean of those distances, of 735 ± 60 pc, and combine that with the the proper motion of $(-2.567, 2.082)$ mas/yr to calculate the velocities.

To see whether we could constrain the distance through scintillation, we tried separate fits with each of these three distances. We found that we could not; all that changes is the fitted screen velocity (proportionally to distance). This is not surprising, since constraining the distance requires constraining the pulsar angular orbital velocity, but for a nearly edge-on orbit and a nearly one-dimensional screen, this is highly degenerate with the angle ψ_{AR} between the screen and the orbit[2], which we cannot constrain well at all.

---

[2] For an overview, see https://screens.readthedocs.io/en/latest/ #modelling-scintillation-velocities.

Apart from the distance, the fits yield consistent results for all other properties of the screen: a fractional distance from the pulsar $s \simeq 0.7$, a high anistropy of $R \simeq 0.9$, a roughly N-S orientation, and a perpendicular velocity of $v_\perp \simeq -25$ km/s. These values consistent with those of R14.

In all cases, the nominal parallel screen velocity is rather large but also is much more uncertain than the perpendicular velocity, as expected for anisotropic screens. To test whether a large parallel screen velocity is required to obtain a good fit, we set $V_{\mathrm{IS},\parallel} = 0$ km/s and repeat the analysis. Using the Akaike Information Criterion (AIC), we find that large velocities are not required: fits with $V_{\mathrm{IS},\parallel} = 0$ km/s are indeed worse but not by much, with the AIC increased from 121 to only 125 in the $i = 89.35°$ case (and from 137 to 146 for $i = 90.65°$, and from 117 to 125 with i left free). The fit also gives somewhat different axial ratios (systematically lower, between 0.44 and 0.84) and screen orientations (between 167.6° and 195.8°), but only very slight changes in the perpendicular velocity (between 21.9 km/s and 25.3 km/s) and fractional screen distance (between 0.613 and 0.695). The fact that there is some sensitivity to the parallel velocity suggests the screen is not fully linear (or that there is a contribution from a second linear screen).

We conclude that the dominant screen is anisotropic, and that our parameters of interest, the screen distance, orientation, and perpendicular velocity, are well constrained.
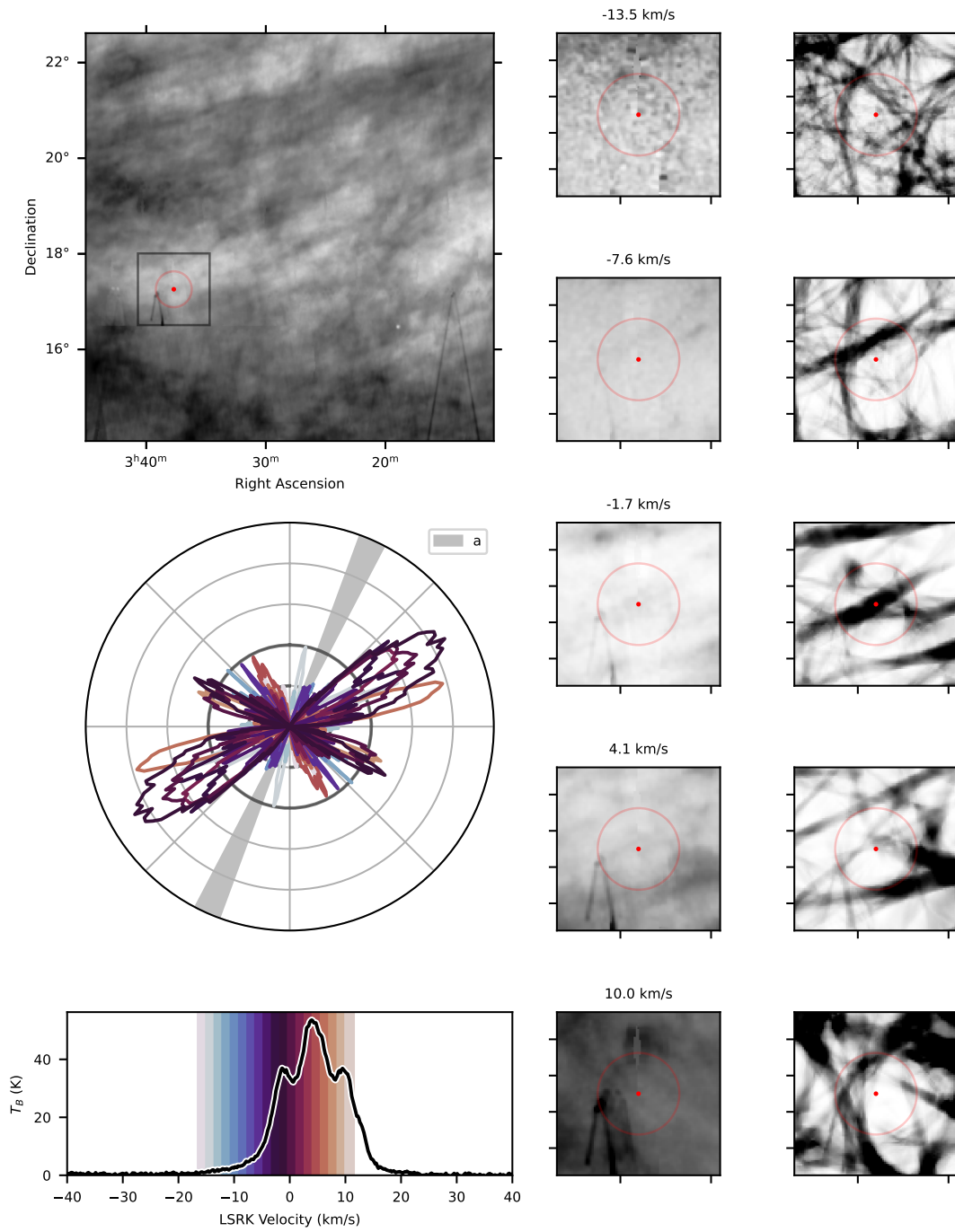
Figure 3. H I filaments near PSR J0337+1715. H I brightness temperature integrated over velocities of −16.5 to 11.5 km/s relative to the kinematic local standard of rest. The identified H I filaments are not aligned with the screen. Layout as in other figures.
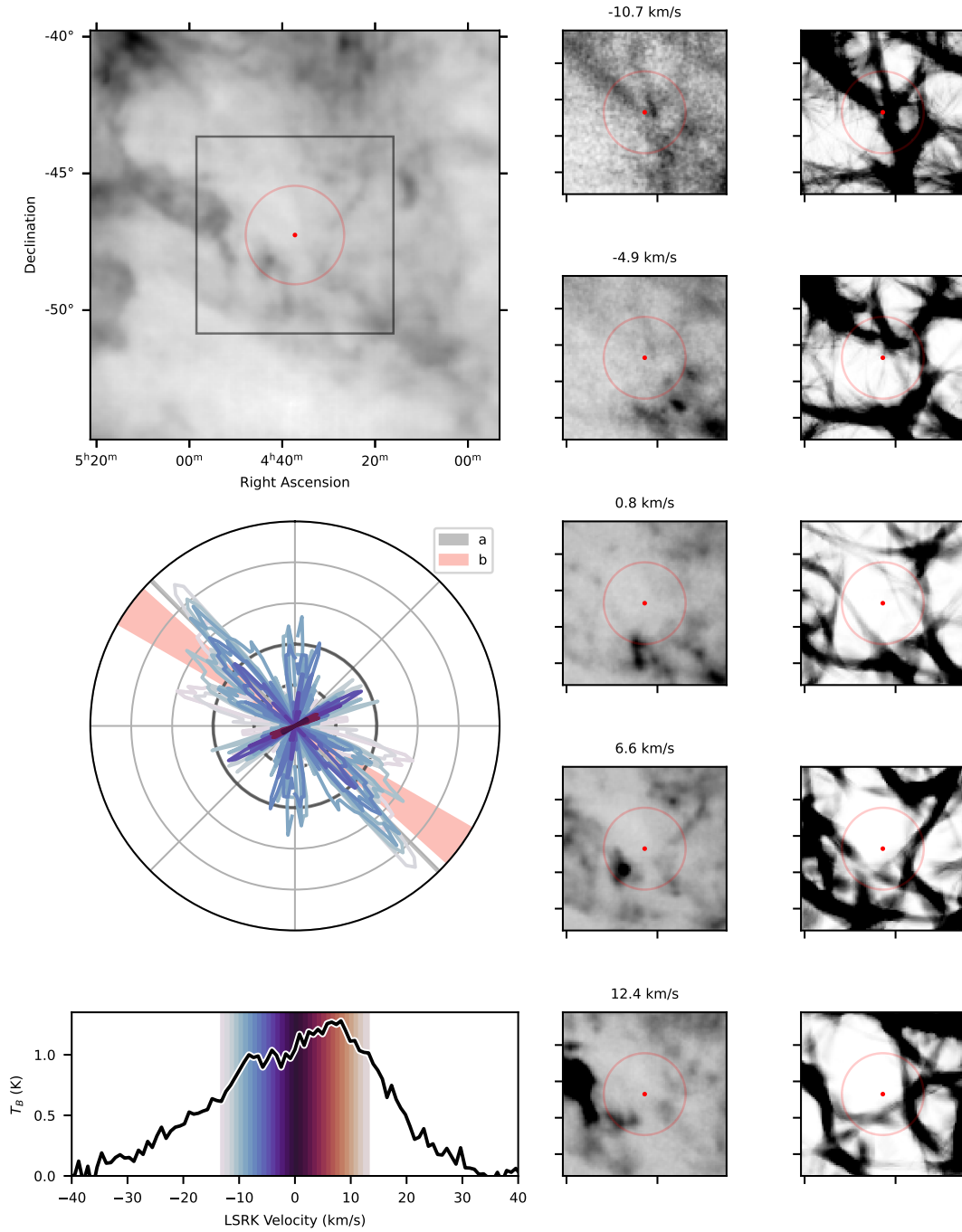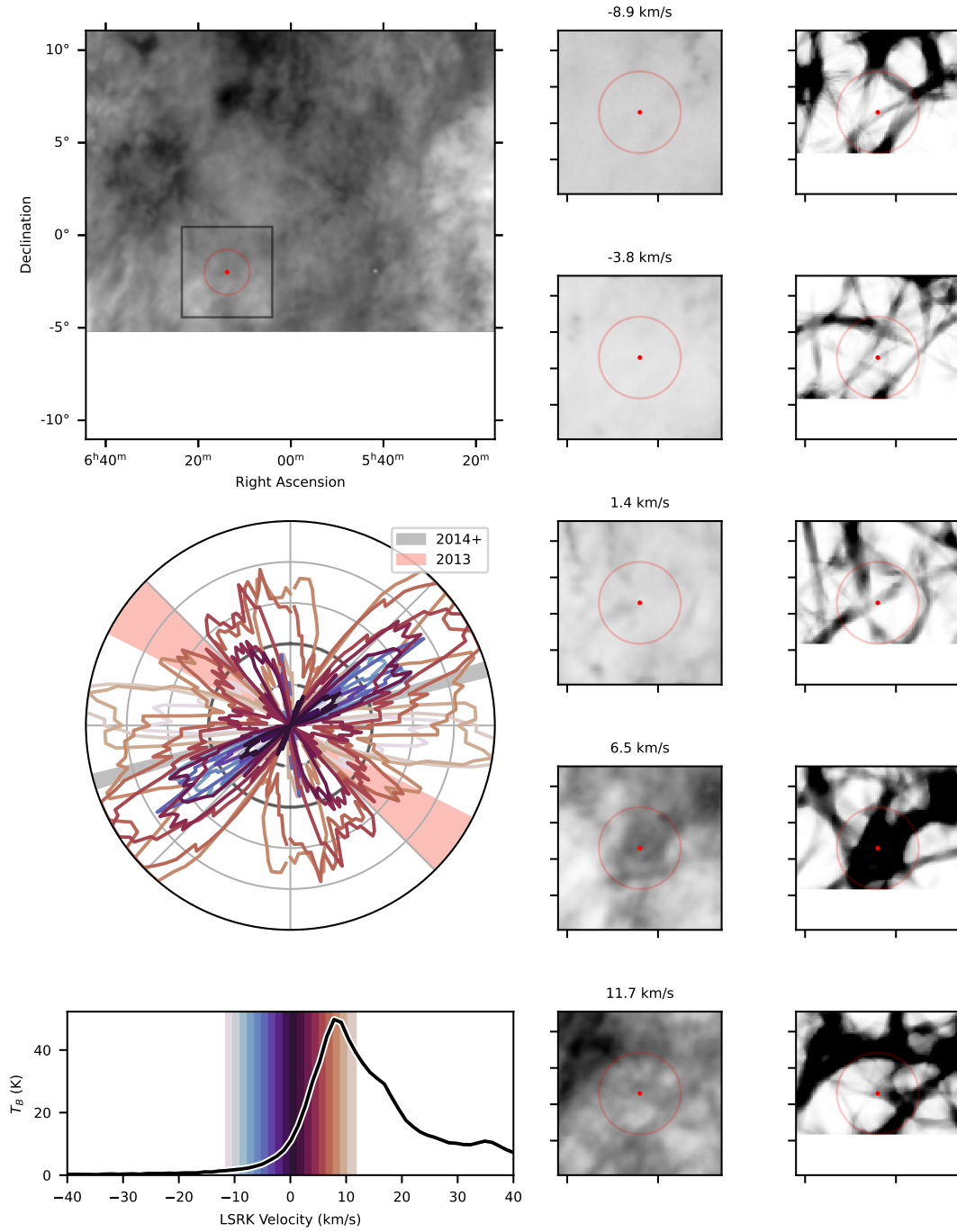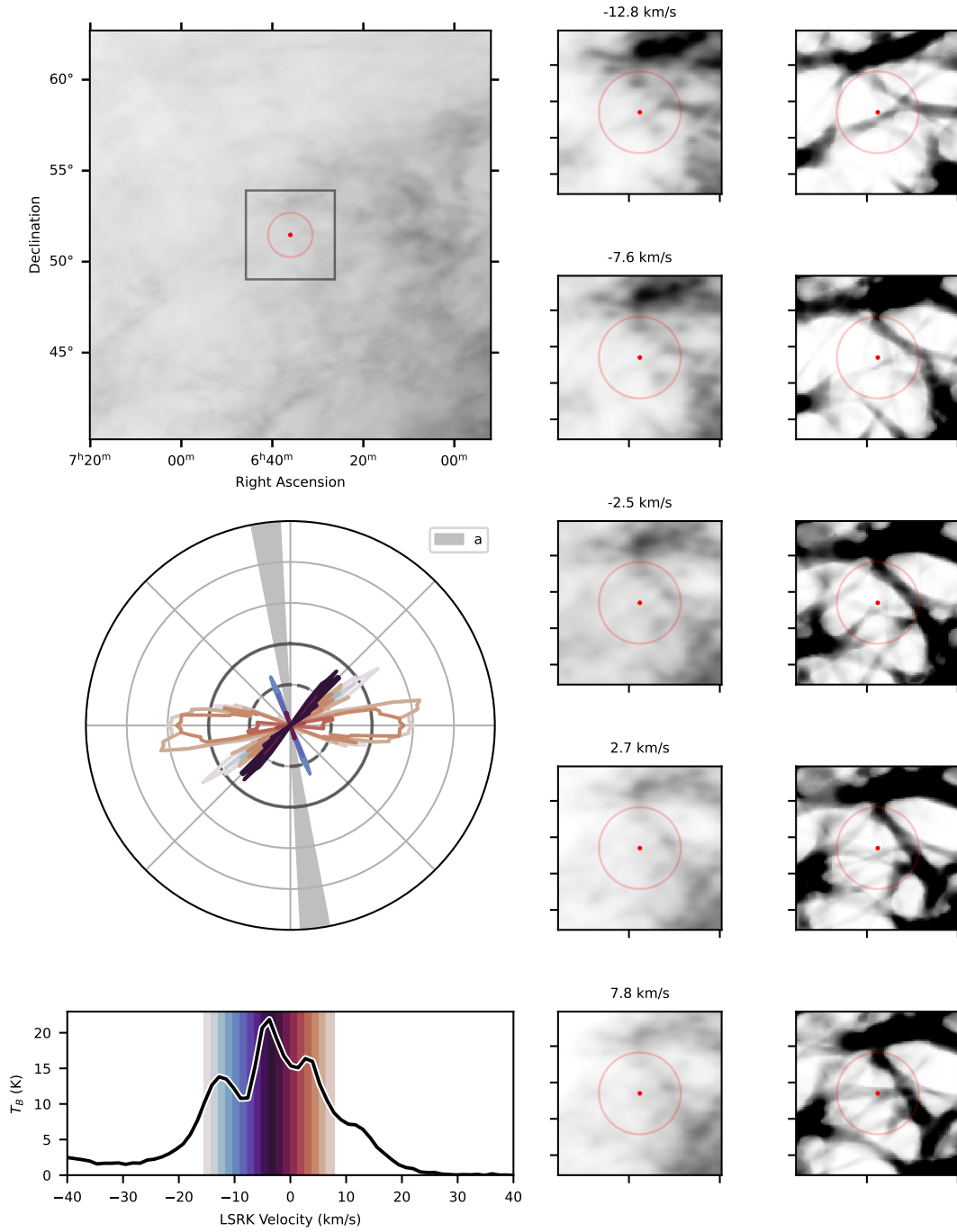
Figure 4. H I filaments near PSR J0437-4715. H I brightness temperature integrated over velocities of -13.2 to 13.2 km/s relative to the kinematic local standard of rest. There is probable alignment of H I filaments with both screens. Layout as in other figures.

Figure 5. H I filaments near PSR J0613-0200. H I brightness temperature integrated over velocities of −11.5 to 11.7 km/s relative to the kinematic local standard of rest. There is probable alignment of H I filaments with both screens. Note there is a cutoff in the H I brightness temperature map due to the declination cutoff of -5° for the EBHIS survey and a similar cutoff in the Rolling Hough Transform backprojections corresponding to one Rolling Hough Transform window from the edge of the H I data. This did not affect the filament measurements at the position of the pulsar. Layout as in other figures.

Figure 6. H I filaments near PSR J0636+5128. H I brightness temperature integrated over velocities of −15.4 to 7.8 km/s relative to the kinematic local standard of rest. The identified H I filaments are not aligned with the screen. Layout as in other figures.
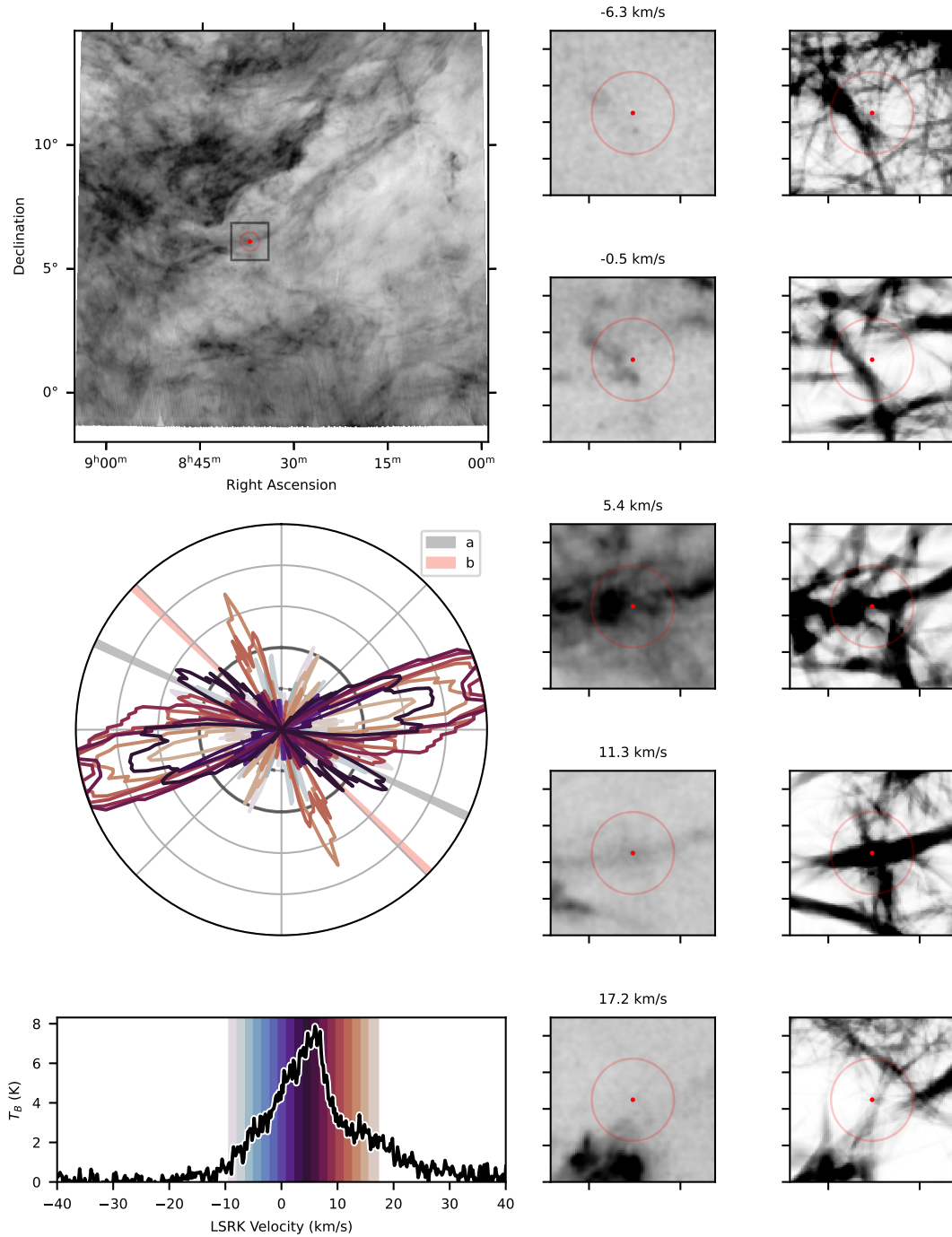
Figure 7. H I filaments near PSR B0834+06. H I brightness temperature integrated over velocities of −9.3 to 17.2 km/s relative to the kinematic local standard of rest. The identified H I filaments are not aligned with either screen. Note there is a cutoff in the H I brightness temperature map due to the declination cutoff of −1.17°. This did not affect the filament measurements at the position of the pulsar. Layout as in other figures.
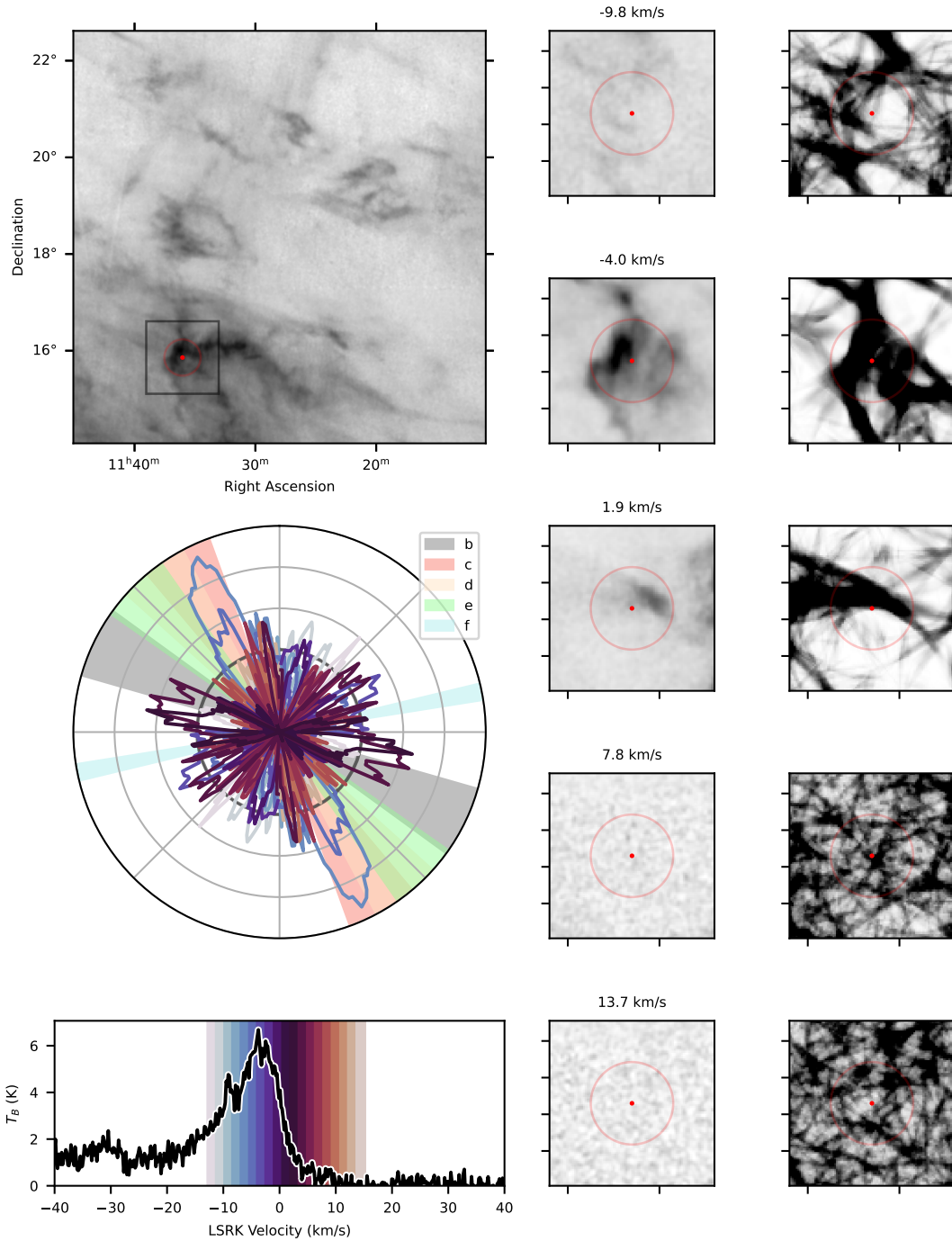
Figure 8. H I filaments near PSR B1133+16. H I brightness temperature integrated over velocities of -12.8 to 15.2 km/s relative to the kinematic local standard of rest. At velocities above 7.8 km/s the emission is dominated by noise. The errors in the orientations of screens c, d, e, and f are shown as $10°$ which is an underestimate of the measurement uncertainties but allows for them to be more easily distinguished from each other. Screens c, d, and e have probable alignment with H I filaments. Layout as in other figures.
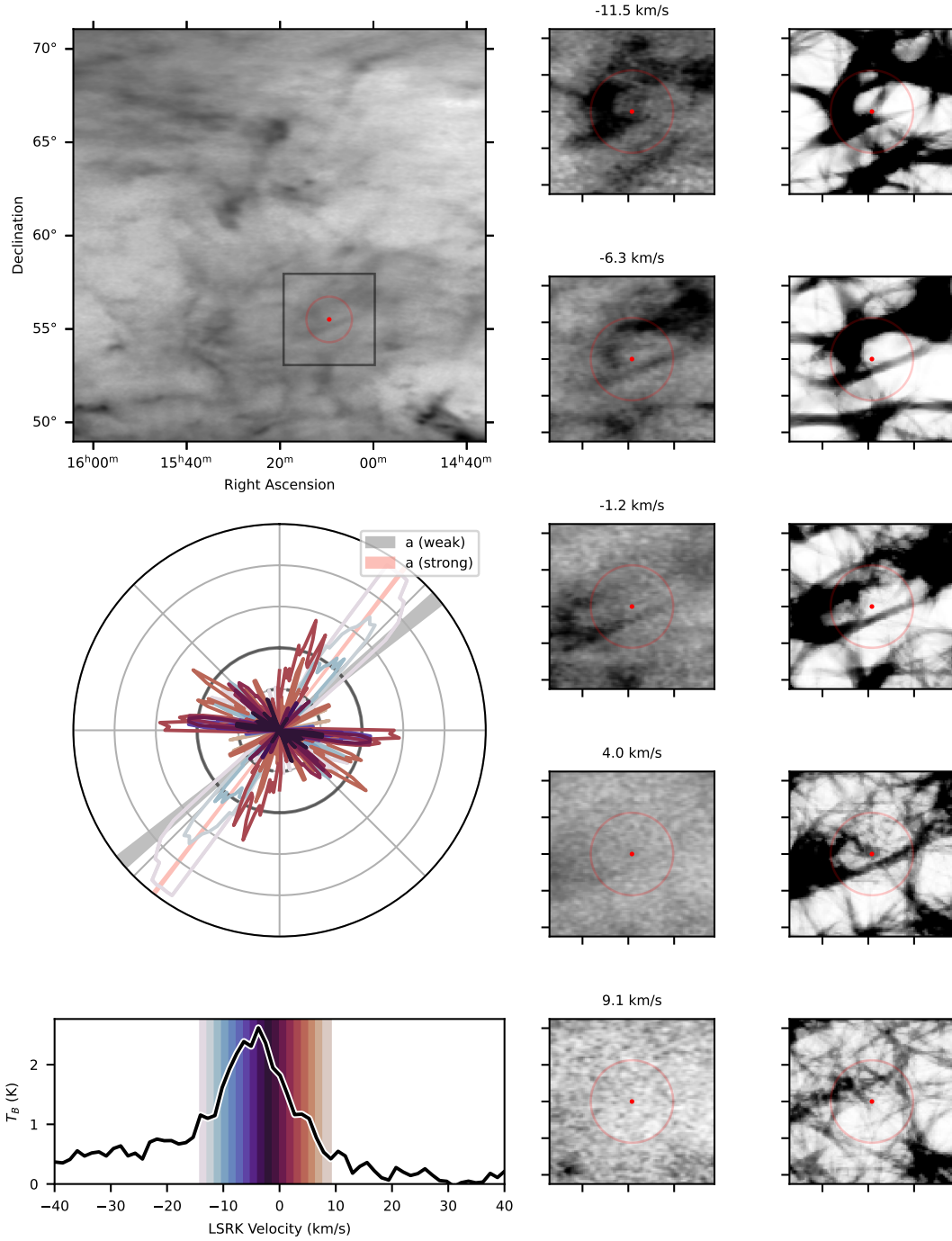
Figure 9. H I filaments near PSR B1508+55. H I brightness temperature integrated over velocities of −14.1 to 9.1 km/s relative to the kinematic local standard of rest. The error in the orientation of the strong scattering screen a is shown as 10° which is an underestimate of the measurement uncertainty but allows for it to be more easily distinguished from weak scattering screen a. There is probable alignment of an H I filament with strong scattering screen a, but not with the other screens. Layout as in other figures.
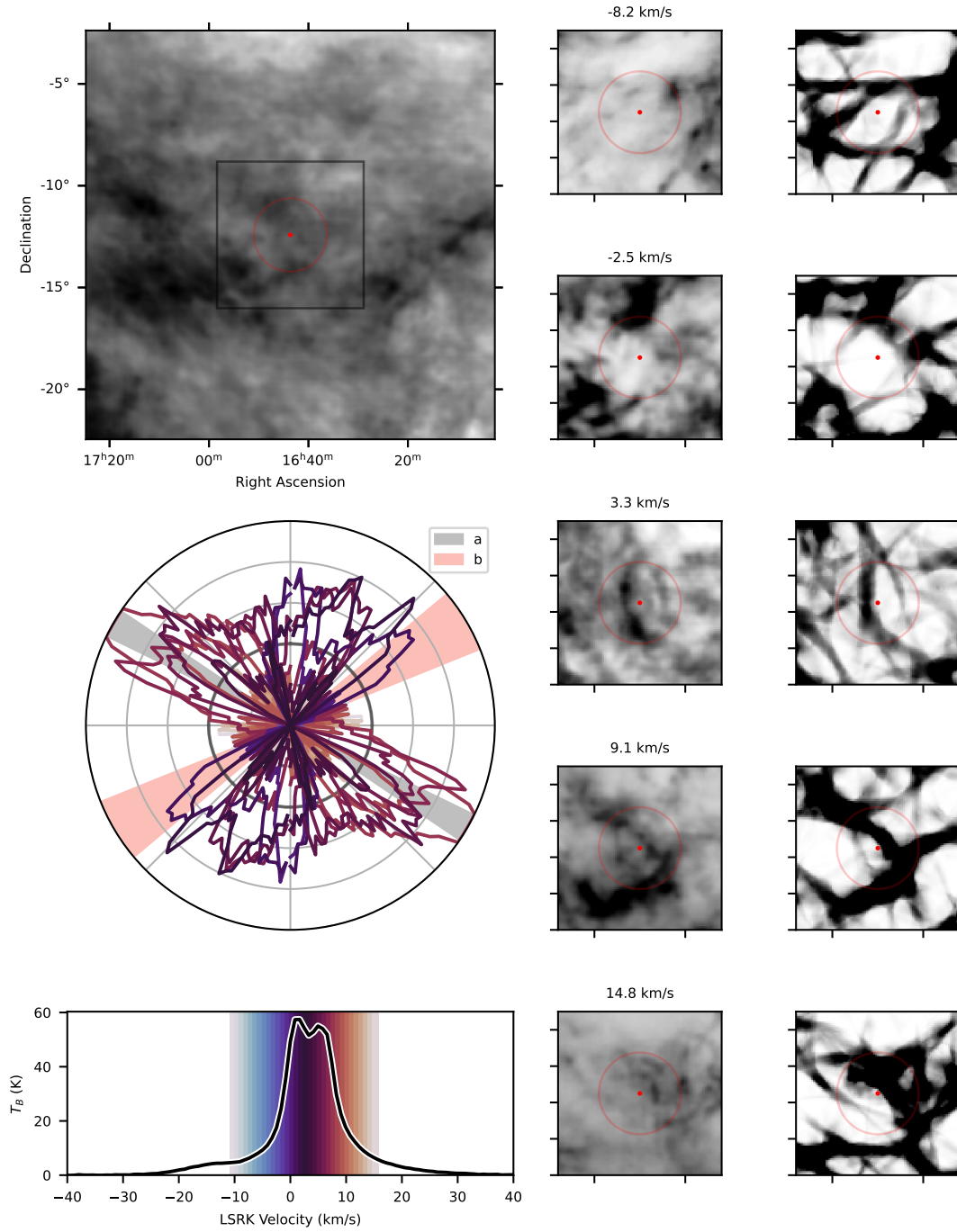
Figure 10. H I filaments near PSR J1643-1224. H I brightness temperature integrated over velocities of -10.7 to 15.7 km/s relative to the kinematic local standard of rest. Both screens have probable alignment with an H I filament. Layout as in other figures.
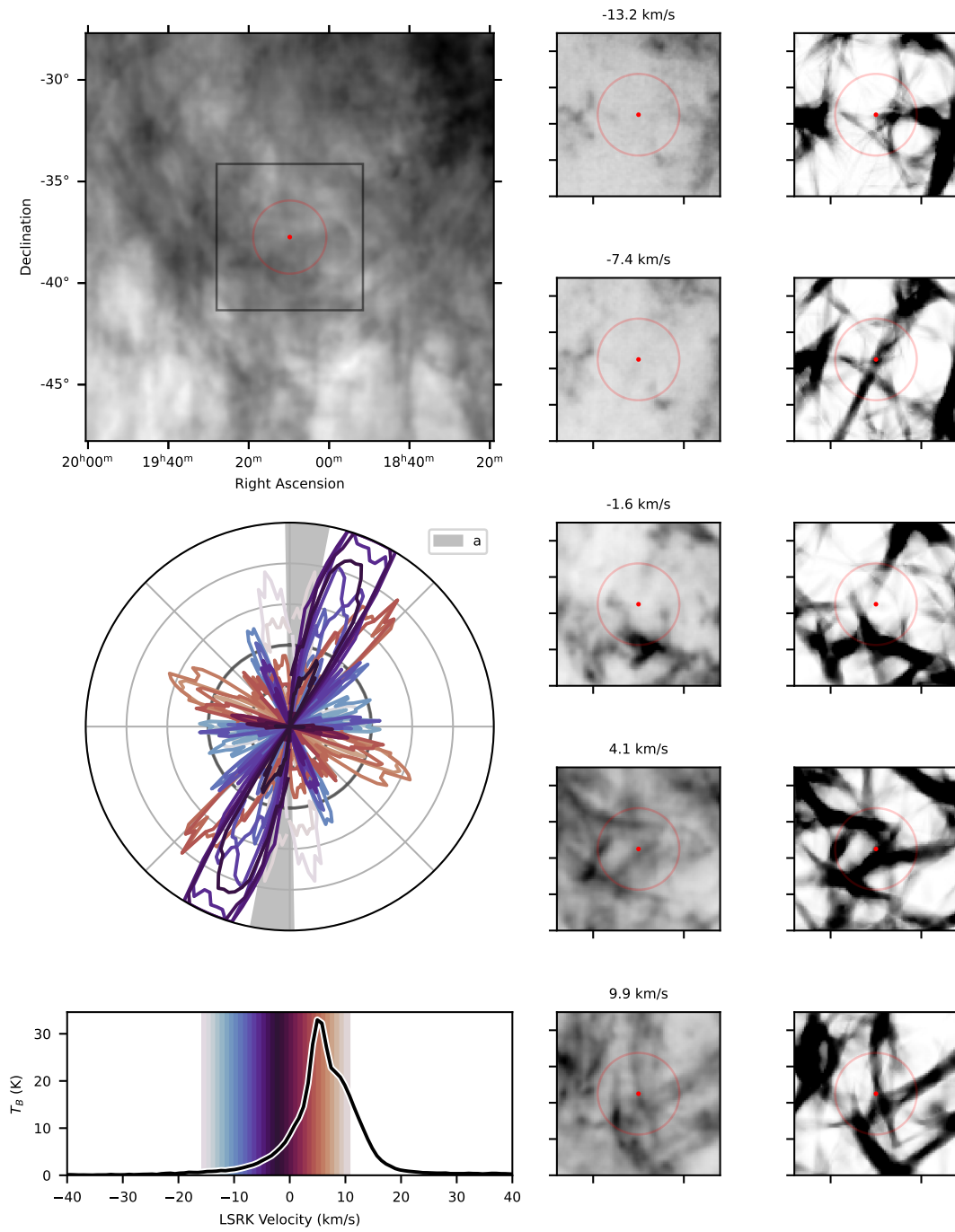
Figure 11. H I filaments near PSR J1909-3744. H I brightness temperature integrated over velocities of −15.7 to 10.7 km/s relative to the kinematic local standard of rest. The identified H I filaments are not aligned with the screen. Layout as in other figures.